

2003

## Structure and Generation of Turbulence at Interfaces Strained by Internal Solitary Waves Propagating Shoreward over the Continental Shelf

J. N. Moum

David Farmer

*University of Rhode Island, farmerd@uri.edu*

W. D. Smyth

L. Armi

S. Vagle

Follow this and additional works at: <https://digitalcommons.uri.edu/gsofacpubs>

---

### Citation/Publisher Attribution

Moum, J. N., Farmer, D. M., Smyth, W. D., Armi, L., & Vagle, S. (2003). Structure and Generation of Turbulence at Interfaces Strained by Internal Solitary Waves Propagating Shoreward over the Continental Shelf. *Journal of Physical Oceanography*, 33, 2093-2112, doi: 10.1175/1520-0485(2003)0332.0.CO;2  
Available at: [https://doi.org/10.1175/1520-0485\(2003\)0332.0.CO;2](https://doi.org/10.1175/1520-0485(2003)0332.0.CO;2)

This Article is brought to you by the University of Rhode Island. It has been accepted for inclusion in Graduate School of Oceanography Faculty Publications by an authorized administrator of DigitalCommons@URI. For more information, please contact [digitalcommons-group@uri.edu](mailto:digitalcommons-group@uri.edu). For permission to reuse copyrighted content, contact the author directly.

---

**Structure and Generation of Turbulence at Interfaces Strained by Internal Solitary Waves Propagating Shoreward over the Continental Shelf**

## Structure and Generation of Turbulence at Interfaces Strained by Internal Solitary Waves Propagating Shoreward over the Continental Shelf

J. N. MOUM

*College of Oceanic and Atmospheric Sciences, Oregon State University, Corvallis, Oregon*

D. M. FARMER

*Graduate School of Oceanography, University of Rhode Island, Kingston, Rhode Island*

W. D. SMYTH

*College of Oceanic and Atmospheric Sciences, Oregon State University, Corvallis, Oregon*

L. ARMI

*Scripps Institution of Oceanography, La Jolla, California*

S. VAGLE

*Institute of Ocean Sciences, Sidney, British Columbia, Canada*

(Manuscript received 19 September 2002, in final form 17 March 2003)

### ABSTRACT

Detailed observations of the structure within internal solitary waves propagating shoreward over Oregon's continental shelf reveal the evolving nature of interfaces as they become unstable and break, creating turbulent flow. A persistent feature is high acoustic backscatter beginning in the vicinity of the wave trough and continuing through its trailing edge and wake. This is demonstrated to be due to enhanced density microstructure. Increased small-scale strain ahead of the wave trough compresses select density interfaces, thereby locally increasing stratification. This is followed by a sequence of overturning, high-density microstructure, and turbulence at the interface, which is coincident with the high acoustic backscatter. The Richardson number estimated from observations is larger than  $1/4$ , indicating that the interface is stable. However, density profiles reveal these preturbulent interfaces to be  $O(10\text{ cm})$  thick, much thinner than can be resolved with shipboard velocity measurements. By assuming that streamlines parallel isopycnals ahead of the wave trough, a velocity profile is inferred in which the shear is sufficiently high to create explosively growing, small wavelength shear instabilities. It is argued that this is the generation mechanism for the observed turbulence and hence the persistent structure of high acoustic backscatter in these internal solitary waves.

### 1. Introduction

Strongly nonlinear internal solitary waves (ISWs) are a ubiquitous feature of the coastal ocean. They have been observed in moored records, from shipboard measurements and remotely by radar. A nice compilation of *Seasat* synthetic-aperture radar observations can be found in Fu and Holt (1982), including an example from the mouth of the Columbia River, the site of the field

experiment described here. It is generally thought that these waves are generated as a consequence of the interaction of the internal tide with stratified fluid in the vicinity of rough topography such as the shelf break.

Observations associate high turbulence levels with ISWs (Sandstrom et al. 1989; Sandstrom and Oakey 1995; Stanton and Ostrovsky 1998; Duda and Farmer 1999). This implies that all of an ISW's energy is not simply deposited in the surf zone but that a significant portion is lost as it propagates onshore over the shelf. Deposition patterns of nutrients and other materials fluxed across the shelf by ISWs will be affected similarly. As an ISW approaches sufficiently shallow water

---

*Corresponding author address:* Dr. Jim Moum, College of Oceanic and Atmospheric Sciences, Oregon State University, 104 Ocean Admin. Bldg., Corvallis, OR 97331-5503.  
E-mail: jmoum@coas.oregonstate.edu

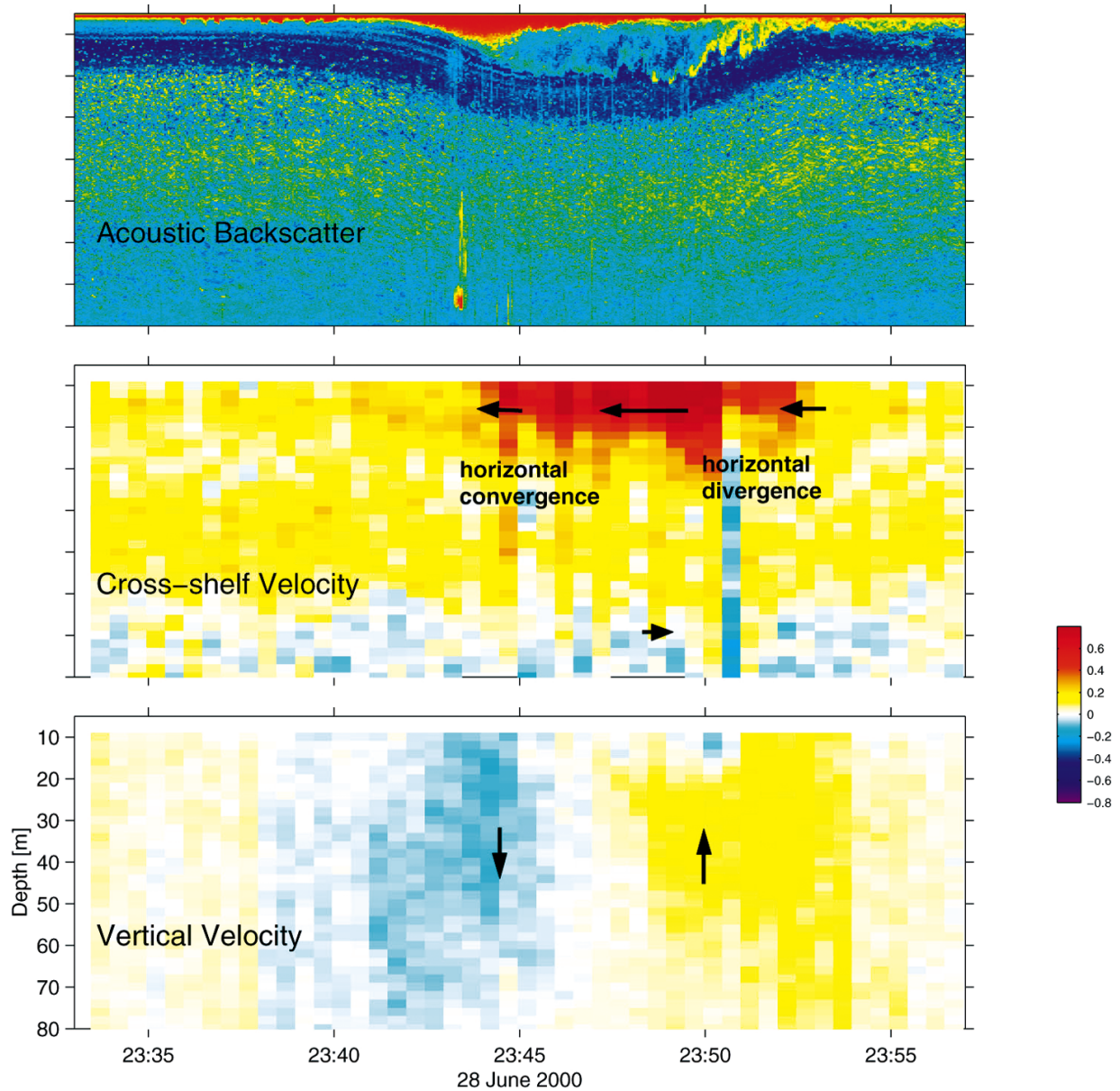


FIG. 1. Time series of acoustic backscatter, horizontal velocity, and vertical velocity made from shipboard while a single internal solitary wave of depression propagated past. Cross-shelf velocity is in the direction of wave propagation. These data were obtained during a pilot experiment in which ADCP velocity data were sampled as 30-s averages. Acoustic backscatter was measured with a high-frequency echosounder mounted in the ship's hull. Arrows represent approximate velocity direction and relative magnitude. Vertical axes are equivalent for each panel, and tick marks in the upper two image plots are referenced in the bottom panel. The scale to the right represents velocity ( $\text{m s}^{-1}$ ).

(i.e., where the wave's amplitude is a substantial fraction of the water depth), breaking may occur as the trailing edge overtakes the wave trough (Vlasenko and Hutter 2002; Kao et al. 1985). However, observation of ISWs in deep water indicate these are also highly turbulent. Pinkel (2000) suggested that ISWs trigger instability of the background current shear in equatorial current regimes, the intrinsic shear of the observed ISWs being too small to reduce local values of the gradient Richardson number below  $1/4$ . From observations over the

continental shelf, Sandstrom and Oakey (1995) associated high turbulence with a highly sheared subsurface interface, although the details of the Richardson number were not clear. Clear evidence of shear instability within ISWs was obtained in acoustic images made in Knight Inlet (Farmer and Smith 1980).

Some basic aspects of internal solitary waves over the continental shelf are evident from observations we made in a pilot experiment off Cape Falcon, Oregon ( $45^{\circ}45'N$ ), in June 2000. Figure 1 shows coincident

measurements of acoustic backscatter and velocity for a typical ISW. This is a wave of depression, supported by stable stratification in a thin layer adjacent to the surface. This time series was initiated with ship adrift and ahead of a shoreward-propagating ISW. The downward vertical velocity ahead of the wave and subsequent upward velocity following the wave indicates the internal fluid motion resulting from the passage of the ISW in its form as a wave of depression. Ahead of the ISW's core (region of maximum velocity), surface currents are convergent above a downwelling subsurface flow. In the upwelling region behind the core, surface currents are divergent. To this point, the description of the velocity structure is identical to that of the theoretical wave discussed by, for example, Lamb (1997) or Lee and Beardsley (1974). Some consequences of this velocity structure are seen in the accompanying acoustic backscatter image. Ahead of the velocity core, the accumulation and downwelling of surface scatterers indicates the velocity convergence there. This region is marked by a distinctive surface signature. On calm days, the convergence zone can be the site of breaking surface gravity waves. More typically, this is the site of enhanced capillary wave activity, visually detected as a twinkling of the surface ahead of the peak current. This signature is clear in X-band (3 cm) surface radar and in L-band (20 cm) satellite radar (Fu and Holt 1982). Also evident in the data depicted in Fig. 1 are 1) enhanced subsurface backscatter at the base of the ISW core behind the wave trough and 2) the irregular nature of the acoustic backscatter interface, especially along the ISW's trailing edge. The enhanced backscatter and complex interface structure indicate turbulence within the ISW.

To further investigate the internal structure of ISWs, we conducted a more extensive experiment off the Oregon coast over three weeks in September–October 2001. A previous investigation of ISWs was conducted in the same region in September–October 1995 (Stanton and Ostrovsky 1998; Kropfli et al. 1999). Although we had observed strong ISWs earlier in 2001 farther south off Newport, Oregon (44°37'N), only weak ISWs were observed there in September 2001, presumably due to weaker stratification following the upwelling season. In September 2001, the largest amplitude ISWs were observed southeast of the mouth of the Columbia River (Fig. 2). Here, the near-surface stratification was strong across the continental shelf and maximum ISW amplitudes of 40 m were observed.

In this paper, we describe the observational methods used (section 2), present a general interpretation of the observations (section 3), and then focus on the nature of turbulent interfaces in the wave—in particular the small-scale compressive strain evident in the finely resolved density profiles. We demonstrate the sequence of events leading to turbulence at the interfaces (section 4) and quantify the mixing through the interfaces. We then examine the nature of the instability at the inter-

faces (section 5). Because our velocity observations do not resolve the small-scale compressive strain detected from our density measurements, we infer a velocity profile in the wave by matching streamlines and isopycnals. Linear stability analysis applied to the inferred velocity and observed density profiles indicate the potential for explosively growing, small wavelength shear instabilities in generating interfacial turbulence. A discussion (section 6) and conclusions (section 7) follow.

## 2. Observations

Our observations were made using the combination of shipboard 300-kHz acoustic Doppler current profiler (ADCP), X-band (3 cm) radar, tow-yoed CTD, 120-kHz narrow-beam echosounder, and our freely falling turbulence profiler, Chameleon (Moum et al. 1995). As well, several aircraft flights were made to track the positions and movement of the ISW fronts.

The ADCP was sampled using 2-m vertical bins and 5-s averages. This rapid sampling permitted detailed observations of the velocity structure of solitary waves. However, this high sample rate also aliased (rather than averaged) the swell velocity into the signal, which is especially apparent in the vertical velocity component of data obtained while the ship was drifting.

Two 120-kHz echosounders were mounted in the transducer well of R/V *Wecoma*, only one of which pinged. They were jointly triggered and both listened for the return signal. The data described here were obtained using the passive unit, sampled at 40 kHz. The resulting vertical resolution is about 0.04 m. The echosounder has a finite beamwidth ( $\frac{1}{2}$  beamwidth,  $\theta = 3^\circ$ ). The horizontal resolution is  $2r \tan \theta$ , where  $r$  is the range. At 30-m range, this corresponds to a 3-m blurring of the image, meaning we cannot distinguish scales smaller than this.

A digital camera was set up to photograph the X-band radar on *Wecoma's* bridge. This provided ancillary data to reinforce real-time visual observations of the sea surface. These observations were used to determine both the orientation of wave fronts and the location of individual ISWs in the group.

Our typical mode of operation was to use the echosounders as reconnaissance tools, steaming offshore and back onshore to locate ISWs. Having identified the clear signature of an evolving ISW from the echosounder, we then followed it onshore. At typical wave propagation speeds of 0.6–0.8 m s<sup>-1</sup> ( $\approx 1.5$  kt), it was straightforward to leapfrog the ISW, traversing it while steaming both on- and offshore at 6–8 kt, many times the wave speed (thereby yielding a cruise track as shown in Fig. 2). To obtain intensive in situ measurements, we positioned the ship ahead of the ISW and drifted, permitting the ISW to propagate past us while we deployed CTD and Chameleon.

The CTD well on R/V *Wecoma* is located amidship, close to the alongship location of echosounders and

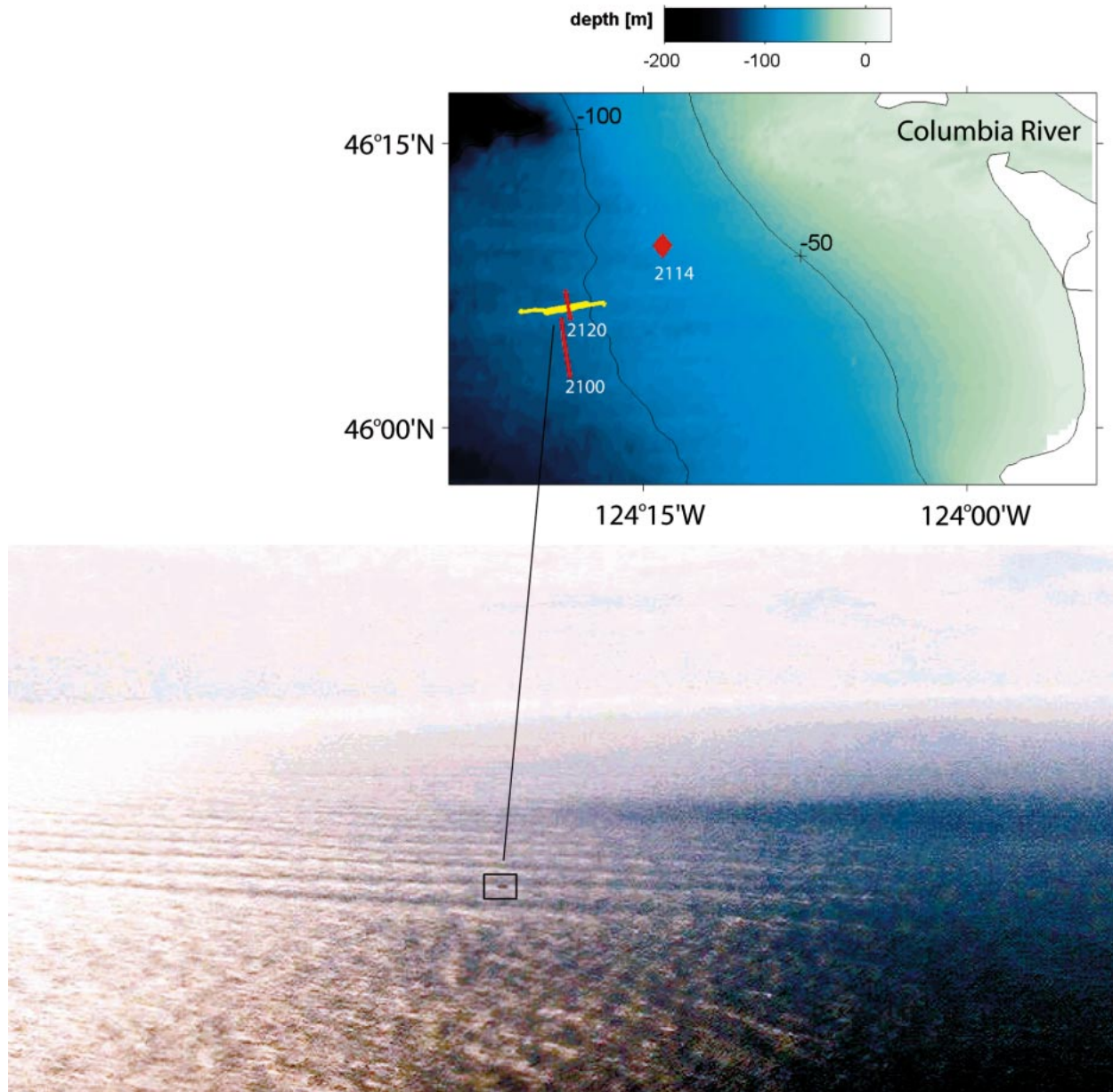


FIG. 2. (top) Location of experiment off the Oregon coast southwest of the mouth of the Columbia River (50- and 100-m depth contours are labeled). The ship's track over the period 2000–2200 GMT 01 Oct 2001 is shown in yellow; this is the period during which most of the observations discussed in this paper were made. During this period, a coordinated aircraft flight was made both to track wave fronts and to photograph the surface signature of ISWs. The photograph at bottom was taken from the aircraft at the location of the red diamond at 2114 UTC (times are noted in white). Aircraft tracks along the wavefront before and after the photograph was taken are shown in red. The longer track is 7 km, and the shorter one is 3 km. (bottom) The R/V *Wecoma* is bounded by the box in the photograph. Alternating bright and dark bands in the photograph are a consequence of ISW-induced convergence (bright, due to enhanced capillary wave field) and divergence (dark, due to reduced capillary wave field).

ADCP. CTD tow-yos executed during the passage of internal solitary waves were typically made to 50-m depth. The freely-falling profiler, Chameleon, was deployed from the fantail. Sensors included those to measure small-scale temperature and conductivity as well as velocity gradients [from which the viscous rate of dissipation of turbulent kinetic energy  $\varepsilon$  was estimated using the method described by Moum et al. (1995)].

### 3. General properties of observed internal solitary waves

For the purpose of this investigation, we followed a typical packet of ISWs as it propagated onshore along  $46^{\circ}06'N$ . In particular, we examine the details of the leading wave. The sequence of ISWs at  $124^{\circ}18'W$  in 109 m of water is shown in Fig. 3, in which the leading

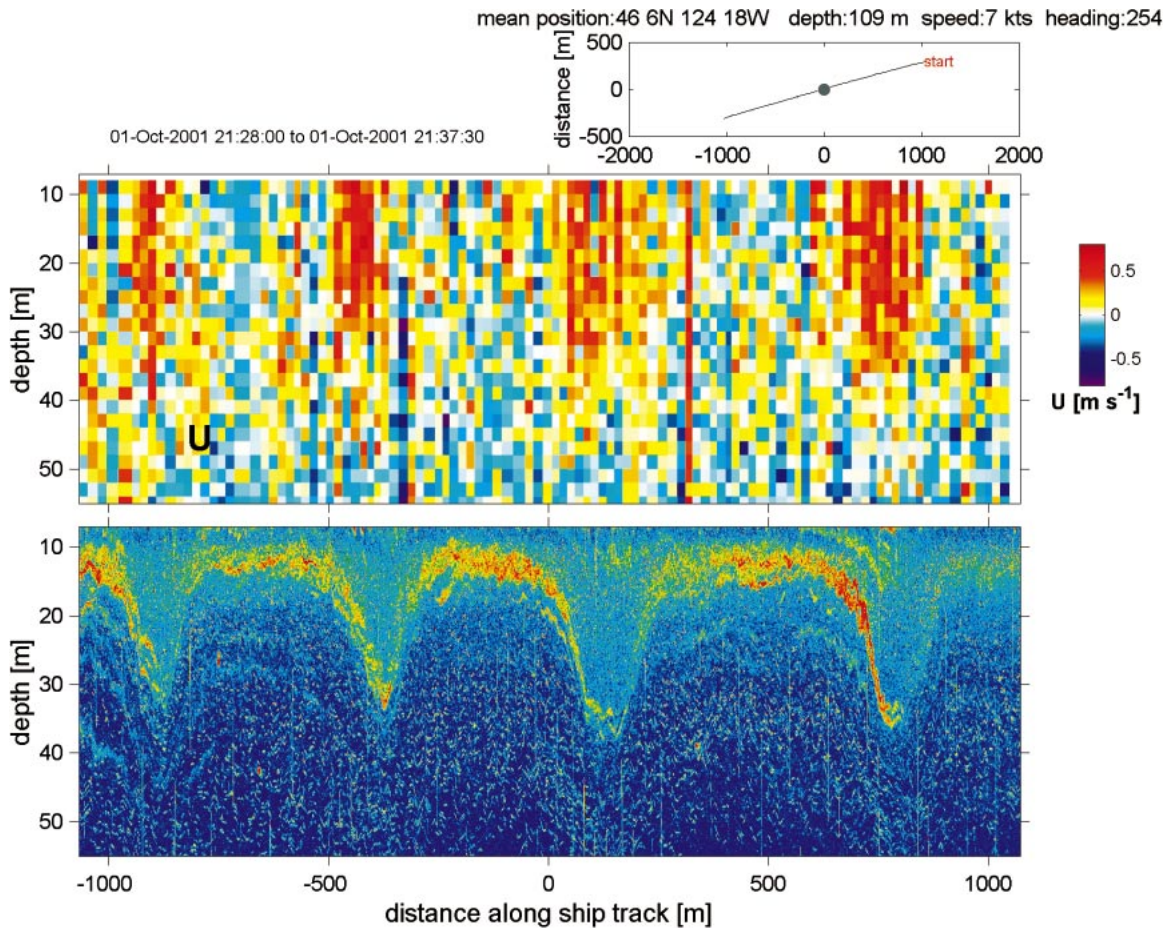


FIG. 3. A sequence of internal solitary waves propagating from left to right in the compass direction 074. These data were obtained while the ship steamed at 7 kt in the direction 254, as indicated above the track plot in the upper-right-hand corner (the track starts at upper right of track line). The track plot shows the mean position (dot at center of track line), water depth, and relative distance along the track (both north-south and east-west). The upper image represents horizontal velocity from the ADCP projected onto the direction perpendicular to the wave fronts as determined from both visual observations and X-band radar, which is the direction the ship is either steaming to or from. This convention is used throughout this paper, including the horizontal velocity image plots shown in Figs. 5, 6, and 7. The lower image is the acoustic backscatter intensity from the 120-kHz echosounder, colored so that red indicates high intensity and blue indicates low intensity.

wave is farthest right.<sup>1</sup> The direction of the transit across the wave train was prescribed from shipboard visual and radar observations (Fig. 4) to be perpendicular to the wave fronts, or parallel (or antiparallel) to the direction the waves were propagating. The spatial extent of the wave fronts is revealed by aircraft flights along them to be many kilometers. The perpendicular tracks of aircraft and ship in Fig. 2 confirm the ship's transit perpendicular to the wave fronts. In the example shown in Fig. 3 measurements were made while the ship was heading offshore, intercepting the shoreward-propagating wave, and so the wave appears foreshortened. The average propagation speed of the wave was determined by track-

ing the leading wave for 20 km as it propagated onshore and is estimated to be  $0.6 \text{ m s}^{-1}$ . The maximum velocity in the wave is close to the wave propagation speed of  $0.6 \text{ m s}^{-1}$ . Because the ship speed is about 5 times the wave propagation speed, observed wavelengths are about 20% smaller than actual.

A persistent feature of the individual ISWs in Fig. 3 is the structure of intense (red) acoustic backscatter associated with these waves. In particular, the backscatter is most intense behind the wave trough and in the wake of each wave. An image (Fig. 5) of the leading wave 5 min previous to that shown in Fig. 3 (and while steaming onshore, thereby Doppler shifting the wavelength to larger scale) shows this structure in more detail. The band of intense backscatter is coincident with the high-shear region at the base of the maximum currents in the ISW core. Backscatter is continuous from the location of the maximum wave depression, through the wave's trailing edge and in its wake.

<sup>1</sup> Throughout this paper, the  $x$  coordinate is defined as the direction of ISW propagation, which is generally within  $20^\circ$  of eastward;  $u$  denotes the corresponding velocity component. The vertical coordinate  $z$  is negative downward from the ocean surface, but plots are labeled using depth, which is  $|z|$ .

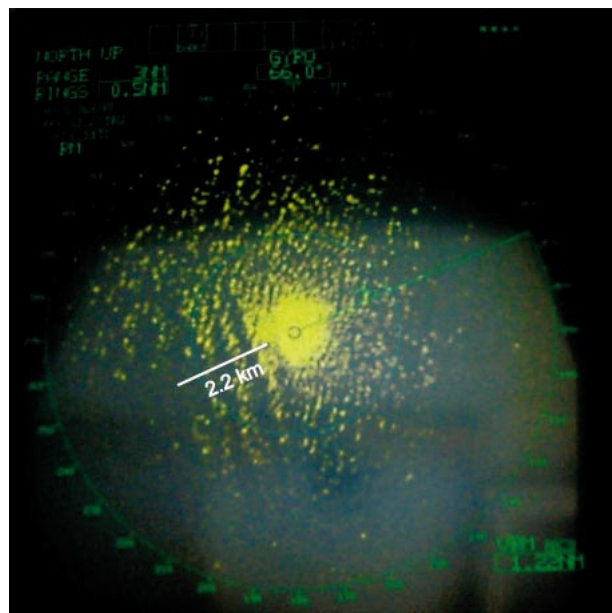


FIG. 4. An X-band radar image photographed at 2119 UTC 1 Oct 2001, coincident with the data shown in Fig. 5. Alternating bands of bright and dark radar reflectivity indicate the surface expression of a sequence of ISWs astern of the ship as the ship steamed in the direction 071 (course made good; ship gyro readout on the radar screen indicates ship heading to be 066 to achieve this course). The leading edge of the leading wave has just been passed at the time of this image.

Having imaged the ISW train many times as we transited across it, we stopped ahead of the wave and allowed it to pass us as we deployed profiling instrumentation to examine the structure in detail (Fig. 6). As the wave passed by, the drifting ship was carried by the wave-induced surface currents, thereby distorting our perception of the wave's form.<sup>2</sup> The main difference in the backscatter image shown in Fig. 6 is the high near-surface intensity not seen in Figs. 3 and 5. This is presumably due to preexisting scatterers and is not associated with the internal structure of the ISW. As the ISW passed, these near-surface scatterers were drawn downward several meters from the surface.

This sequence of images (Figs. 3, 5, and 6) was made over a 1-h period as the leading wave progressed almost 2.5 km toward the shore in a direction 15°–20° north of east as the bottom shoaled from 109- to 99-m depth. During this period and over this transit, the high acoustic backscatter at the sheared interface at the base of the ISW core beginning just ahead of the wave trough remained a persistent signature. While we followed the ISW farther onshore, this persistent signature became obscured by preexisting scattering layers through which the ISW propagated.

The depression of acoustical scattering surfaces cor-

responds closely with isopycnal displacements (Fig. 7). For this comparison, we use the density from the towed CTD as it profiled directly beneath the echosounder. (Chameleon was deployed from the starboard quarter and, since it is lighter than the CTD package and it falls relatively freely, does not fall directly beneath the ship.) Chameleon provides a quantitative measure of the turbulence within the ISW. As the ISW progressed past the drifting ship,  $\epsilon$  increased in two distinct regions (Fig. 7). Between 7- and 15-m depth,  $\epsilon$  was low ahead of the ISW but increased 2–3 orders of magnitude above the ISW velocity core.<sup>3</sup> This intense near-surface dissipation subsided in the wave's wake and then resumed as the second wave passed. The dissipation rate also increased significantly at the sheared and stratified interface at the base of the ISW core, beginning at 2223 UTC and 32-m depth. This increase in  $\epsilon$  continued through the maximum depression and the trailing edge of the wave. It is also apparent to a lesser degree in the second wave and coincides with the bright band of high acoustic backscatter intensity there.

#### 4. Interface structure, evolution, and mixing

A sequence of Chameleon profiles made ahead of the ISW shown in Fig. 7 and through to its maximum depression indicates the rapidly changing structure of the water column (Fig. 8). The first profile shown here (in blue) was made ahead of the wave; the final profile (red) was made at the point of maximum wave depression. Isopycnal displacements ( $\eta$ ) were computed relative to isopycnal depths in the initial profile. The vertical displacement of the  $\sigma_\theta \sim 24.6$  isopycnal, located at 13-m depth ahead of the wave, is in excess of 20 m. The vertical structure of  $\eta$  is predominantly mode 1. On the mode-1 scale, above the maximum displacement, isopycnals are spread apart ( $d\eta/dz < 0$ ) as the wave passes; below the maximum displacement, isopycnals are squeezed together ( $d\eta/dz > 0$ ).

The  $\eta$  profiles also indicate structure on scales much smaller than mode 1. This can be a consequence of both turbulent overturns and straining by the passage of the ISW. To look more closely at the vertical structure requires that we focus on potential temperature ( $\theta$ ) rather than density (which is not resolved as well as  $\theta$  from these measurements). Shown to the lower left in Fig. 8 is an expanded plot of  $\theta$  corresponding to the range in depth and  $\sigma_\theta$  bounded by the dashed box. The interface centered at about 12.4°C progressively sharpens as the wave passes by. It is notably sharpest in the third to last profile, following which an overturn is apparent in the presence of a thin layer of relatively cool (dense) fluid above warmer (lighter) fluid below. This is in turn fol-

<sup>2</sup> Although Fig. 6 is shown here as a time series, it is only so relative to the ship, not to any geographical coordinate.

<sup>3</sup> These image plots begin at 7-m depth. This is 2.5 m below the ship's hull where the acoustic transducers are mounted and is usually below the depth at which ship-induced turbulence is a concern, while drifting.



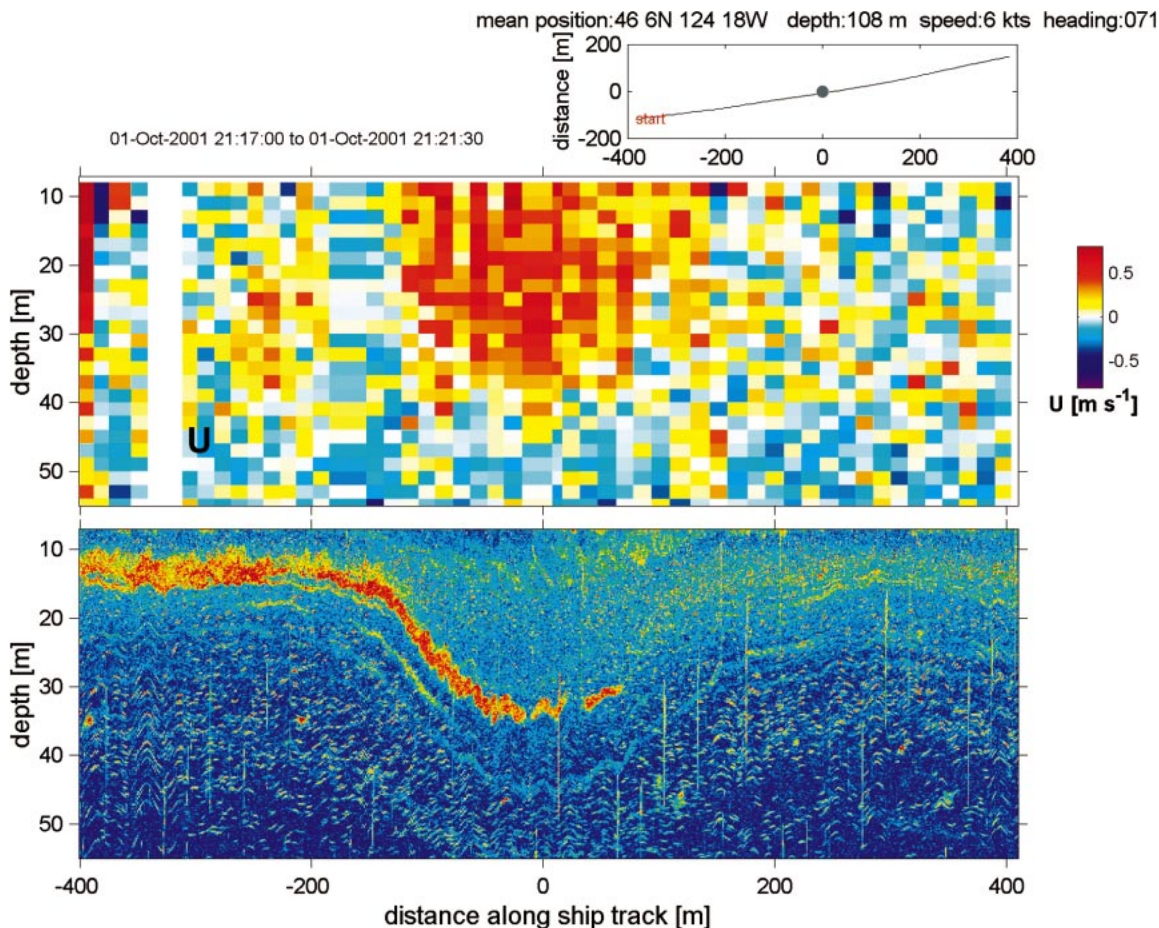


FIG. 5. A single internal solitary wave propagating from left to right. These data were obtained while the ship steamed at 6 kt in the compass direction 071. This is the leading wave in the sequence depicted in Fig. 3 as it appeared 5 min earlier.

lowed in the final profile of the sequence by enhanced small-scale structure, indicative of actively turbulent fluid.

A more complete view of the evolution of the vertical structure and turbulence at this interface as two successive ISWs pass is seen in Fig. 9. Here, the depth has been referenced to its mean value within the  $\sigma_\theta$  range 24.2–25.2, which is plotted as dots on the acoustic backscatter image. We consider this reference frame to represent the time evolution of the interface as the ISWs pass by. Pertinent variables are then plotted as a function of vertical position relative to the instantaneous depth of the interface.

The sequence of profiles through the leading edge and maximum displacement of the first ISW indicates the squeezing of isopycnals ahead of the trough. The interface value of  $N^2$  increases consistently over profiles 4, 5, 6, and 7 as the interface descends.<sup>4</sup> In profile 8, the interface is replaced by a mixed region of thickness  $\sim 1.5$  m, bounded above and below by layers of mod-

erate stratification. Prior to profile 8, turbulent overturns ( $L_T$ ) are nonexistent at and above the interface (although there is some evidence of small overturns below), and there is no strong turbulence indicated in either the record of small-scale temperature gradient ( $T'$ ) or in  $\epsilon$ . Immediately following the maximum interface value of small-scale  $N^2$  in profile 7, overturns develop. The interface then becomes actively turbulent throughout the trailing edge and wake of the wave. A similar, though less energetic, sequence is apparent in the second wave. Here, the maximum increasing interface value of  $N^2$  peaks in profile 19, just before the maximum depression.

The high acoustic backscatter observed at the interface clearly coincides with enhanced temperature microstructure (Fig. 9). The dependence of acoustic backscatter on sound speed fluctuations has been demonstrated by Thorpe and Brubaker (1983) and modeled by Goodman (1990) and Seim et al. (1995). Implementing the form of Seim (1999; at 120 kHz) yields the estimate of volume scattering strength shown in Fig. 10. Here, salinity gradient variance was estimated as the product of temperature gradient variance and the ratio of salinity

<sup>4</sup> Profile 7 is denoted by the black dot in Fig. 9.

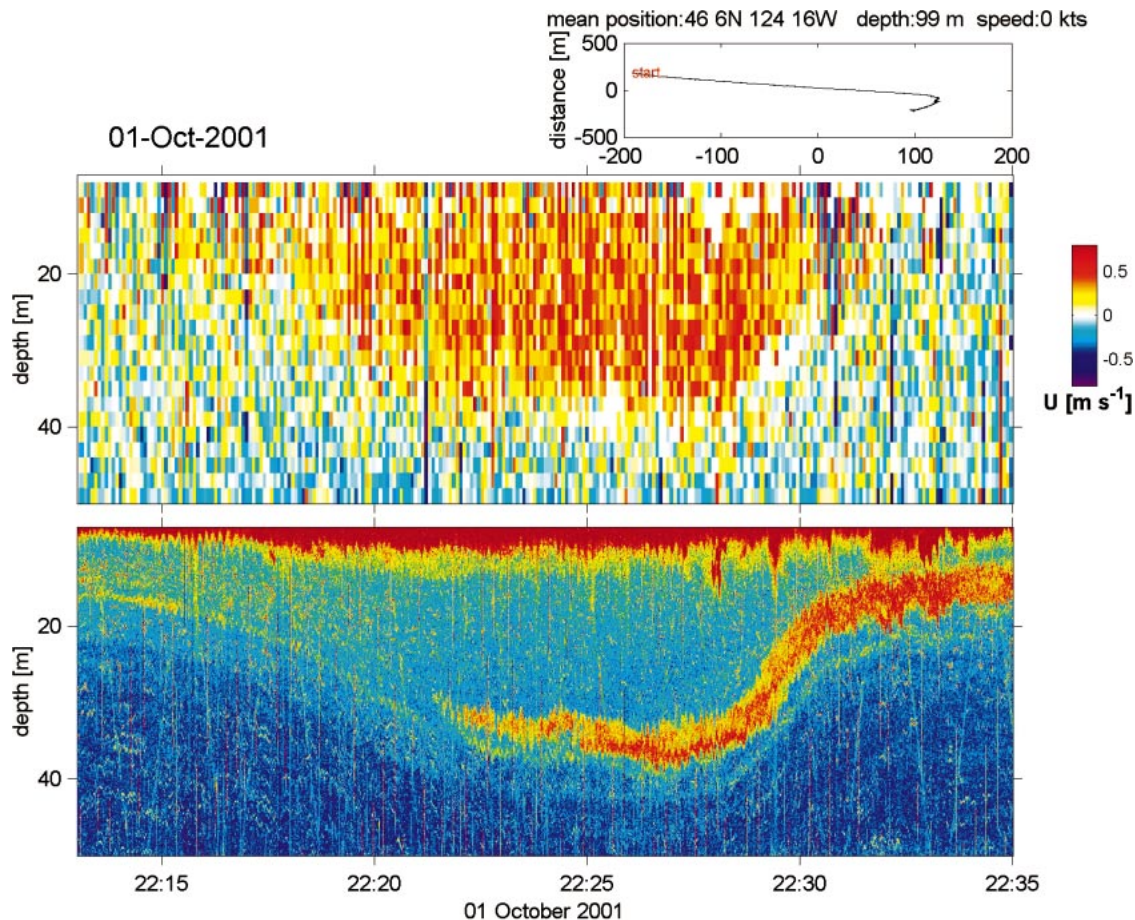


FIG. 6. Echosounder image and velocity structure of the internal solitary wave shown in Fig. 5 1 h later and while the ship is drifting. Observations are plotted as functions of time. The direction of wave propagation is to the left in this perspective. The sawtooth pattern from top to 50-m depth in the echosounder image is the reflection from a tow-yoed CTD deployed on the ship's starboard side at approximately the same alongship location as the hull-mounted echosounder. The ship track (upper right) indicates the influence of the ISW on the ship, which is first carried onshore by the wave current and subsequently carried back offshore by wind and/or current.

to temperature gradients. The microstructure estimate of volume scattering strength is shown in comparison with that calibrated for our echosounder (in which the system of transmitter/receiver is treated as a monostatic system because of the close proximity of the pair). The interfacial peak in observed backscatter is reproduced in the microstructure estimate to within a few decibels. The slight depth misalignment is a function of the spatial separation between echosounder and Chameleon. We conclude that the strong acoustic backscatter observed here is consistent with sound speed fluctuations caused by density microstructure (and note that the contribution of temperature microstructure dominates).

The strong turbulence observed at the high acoustic backscatter interface behind the trough of the ISW suggests that this is a site of enhanced mixing. To quantify this, we use two estimates of the turbulent eddy diffusivity. Following Osborn and Cox (1972),  $K_T = 0.5\chi_T/T_z^2$ , where  $\chi_T$  is the rate of dissipation of temperature gradient variance (estimated from appropriately corrected FP07 thermistor measurements; Nash et al. 1999),

and  $T_z$  is the mean vertical temperature gradient. Our other estimate originates from a production/dissipation/buoyancy flux balance of the turbulent kinetic energy equation in which the buoyancy flux is taken to be a fixed fraction of the dissipation (or the production). This leads to  $K_\rho = \Gamma\varepsilon/N^2$ , where  $\Gamma$  is simply related to the mixing efficiency (Osborn 1980). Here, we take  $\Gamma$  to be 0.2, based on open-ocean evaluations of relatively steady-state turbulence (Moum 1996).

The two turbulent diffusivity estimates are consistent. Results using  $K_\rho$  are shown in Fig. 11. Maximum instantaneous values exceed  $0.1 \text{ m}^2 \text{ s}^{-1}$ , while the mean value through the interface is about  $0.005 \text{ m}^2 \text{ s}^{-1}$ , similar to that observed in an internal hydraulic jump downstream from a small bank on the Oregon shelf (Nash and Moum 2001), and 100 times that observed both upstream of the bank and from other continental shelves (Crawford and Dewey 1989; Sundermeyer and Ledwell 2001). As a result, instantaneous values of the turbulent heat flux through the interface are thousands of watts per square meter. The mean value for the 10-min period

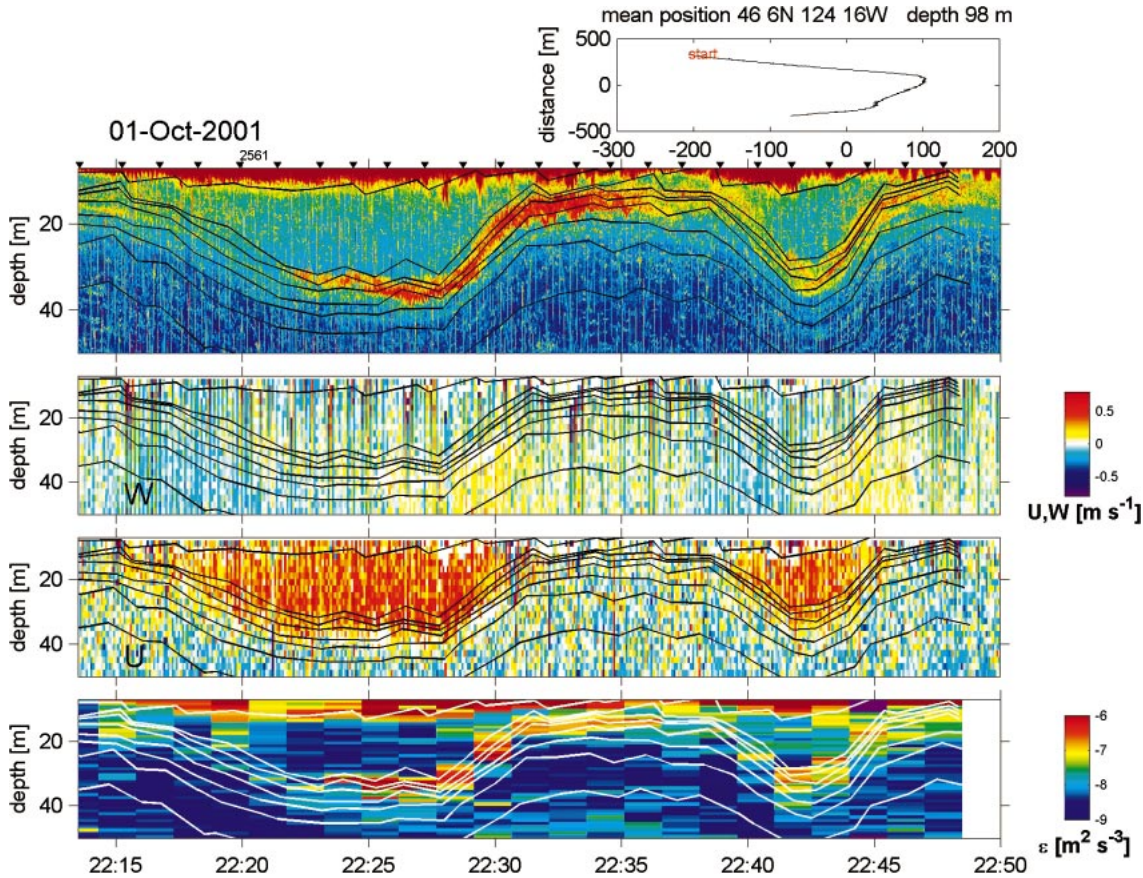


FIG. 7. Echosounder image and vertical and horizontal velocity structure of the first two ISWs in the wave train, the first of which is shown in Fig. 6. The bottom image shows the turbulent dissipation rate as determined from Chameleon profiles. Solid lines on all image plots represent isopycnals determined from tow-yoed CTD. Inverted triangles above the top image indicate locations of Chameleon profiles.

of intense turbulence beginning at the ISW trough is about  $100 \text{ W m}^{-2}$ , during which approximately  $60 \text{ kJ}$  of heat is transported across the interface.

Independent evidence of ISW-induced mixing across an interface is provided by another example in which a kink in the  $\theta$ - $S$  curve upstream of an ISW (blues, greens in Fig. 12) coincides with a strongly mixing interface similar to that in Fig. 9. Downstream of the ISW (reds in Fig. 12), the kink has apparently been mixed away and the  $\theta$ - $S$  curve joins the endpoints along a relatively straight line. The mean value of the turbulent diffusivity through the interface was  $K_p = 0.005 \text{ m}^2 \text{ s}^{-1}$  over the 10-min time period that intense mixing was observed. As an independent test of our estimate of the turbulent diffusivity, we apply the time-dependent diffusion equation

$$\frac{\partial \theta}{\partial t} = K_\theta \frac{\partial^2 \theta}{\partial z^2} \quad (1)$$

to the example  $\theta$ - $S$  profile, where  $\theta$  is intended here to represent either temperature or salinity. Equation (1) is solved numerically with the upstream profiles  $\theta(z)$  and

$S(z)$  as initial conditions and  $K_\theta = K_S = 0.005 \text{ m}^2 \text{ s}^{-1}$ . The diffusion time is 10 min, corresponding to the period of observed intense mixing. The result is the thin black line in Fig. 13. To quantify the uncertainty, the calculation was reproduced with  $K_p = 0.001 \text{ m}^2 \text{ s}^{-1}$  and  $K_p = 0.01 \text{ m}^2 \text{ s}^{-1}$ , with the results plotted as gray lines in Fig. 13. The approximate correspondence between the red and black curves shows that the mean diffusivity estimated using the Osborn (1980) formulation with  $\Gamma = 0.2$  accounts for the observed diffusivity to within a factor of  $\sim 3$ .

## 5. The role of shear instability

Dynamic instability of stratified, parallel shear flows is thought to be a common mechanism for the generation of turbulent overturns in geophysical flows (DeSilva et al. 1996). Smyth et al. (2001) have shown that turbulence in numerical simulations of Kelvin-Helmholtz (KH) instability (i.e., instability of a localized shear layer) is statistically consistent with turbulence in overturns revealed by microstructure profiles in the thermocline.

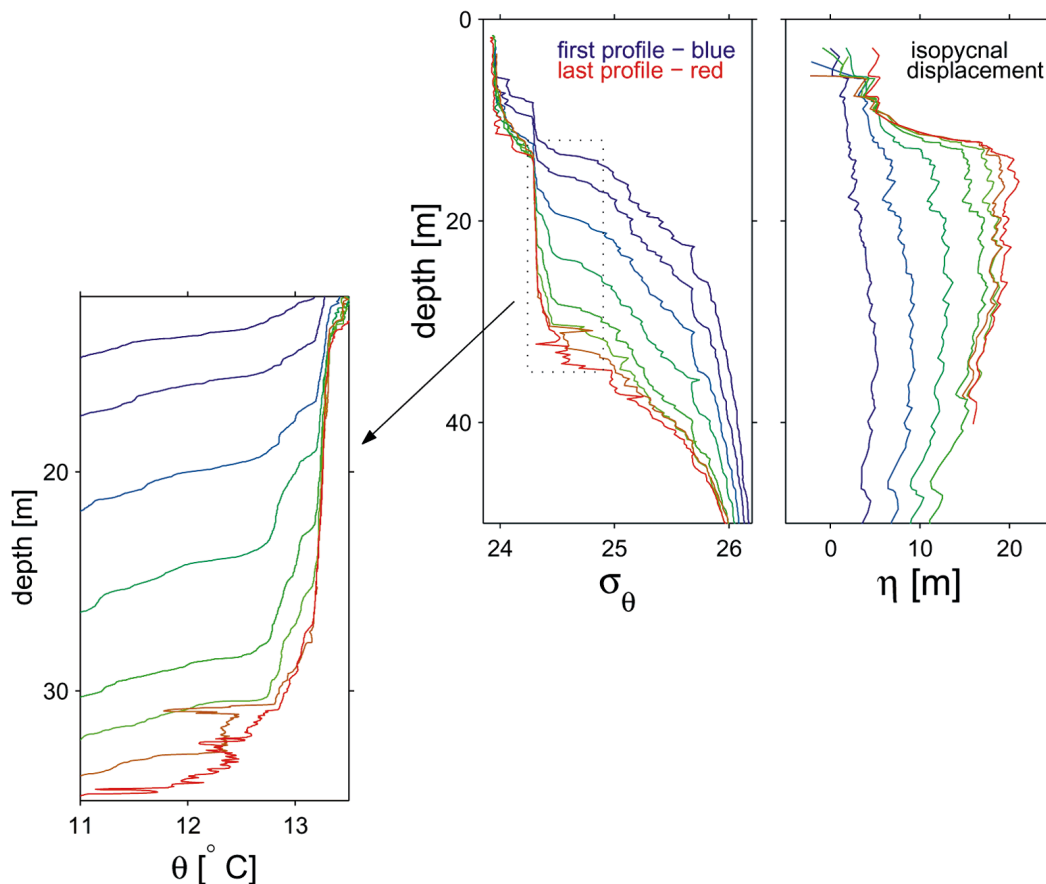


FIG. 8. Vertical profiles of  $\sigma_\theta$  and isopycnal displacement ( $\eta$ ) through the leading edge of the leading ISW depicted in Fig. 7. Displacement is shown as a function of initial isopycnal depth. The first profile (ahead of the wave) is blue and the color sequence goes through green to red marking the final profile at the location of maximum depression. For reference, the profiles shown here are marked by gray or black dots in Fig. 9. At lower left is an expanded plot of potential temperature ( $\theta$ ) for the depth and  $\sigma_\theta$  range shown in the dashed box.

Could shear instability be responsible for the small-scale turbulent overturns described in the previous section?

A vivid illustration of shear instability at work in an ISW is shown in Fig. 14. Beginning at the leading edge of the wave ( $x = 170$  m; depth 12 m, shown by arrow), we see a thin band of enhanced backscatter. About half-way to the wave trough, this scattering layer exhibits wavelike structures suggestive of KH instability. Toward the trough, the scale of the billows increases. This increase is consistent with growth in time. (Here KH billows propagate at the local speed of the background flow; in this case the speed of the ISW-induced flow at the depth where the billows are observed. Because this is less than the wave's propagation speed, billow age increases in the direction opposite to wave propagation, that is, from right to left in the figure.) Just behind the trough we observe two large billows (approximately 10 m high by 50 m long) separated by a patch of small-scale structure. At the trailing edge of the ISW is a final billow whose internal structure is much less organized than the earlier billows, suggesting turbulent breakdown. This sequence of billow structures, interpreted as

a time series, is largely consistent with the growth and breaking of KH billows as revealed in laboratory experiments (e.g., Koop and Browand 1979) and numerical simulations (e.g., Smyth and Moum 2000; Caulfield and Peltier 2000; Smyth et al. 2001). The sole exception to this correspondence is the patch of small-scale structure located between the two large billows just behind the trough. The origin of this structure is the subject of a separate study.

Clear observations of classical KH billows like those seen in Fig. 14 are rare. Another aspect of this backscatter image is quite typical, however, and that is the appearance of thin layers of strong scattering beginning near the ISW trough. An example of such a layer has already been described in section 4. In Fig. 14, two such layers are visible, both located below the large billows. As in the examples described in previous sections, both of these deeper layers are too thin for their structural details to be well resolved in the present measurements, and the cause of the layers is therefore difficult to determine. A possibility that suggests itself immediately is that the thin streaks are, like the large billows, gen-

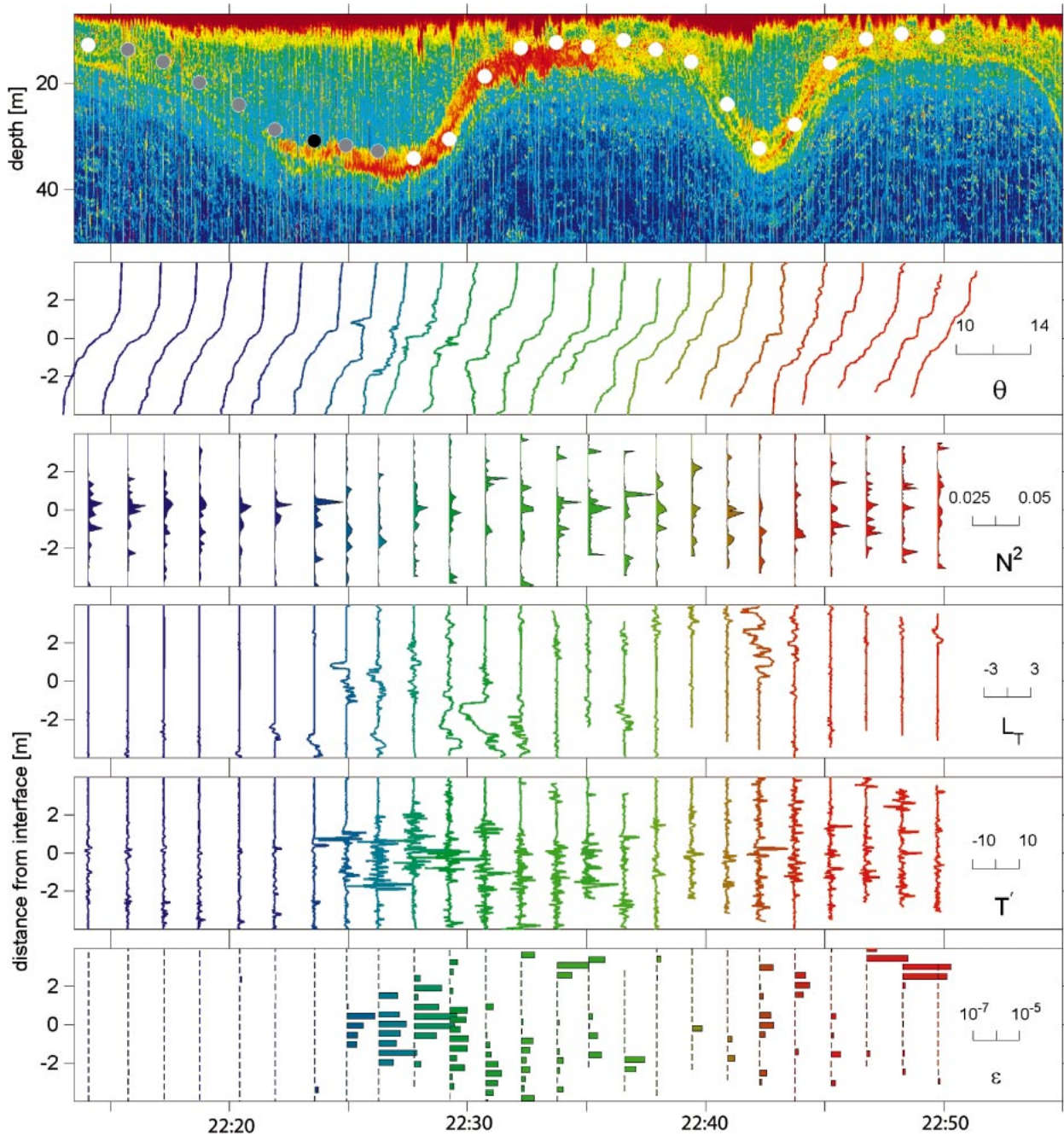


FIG. 9. Sequence of profiles through the ISW depicted in Fig. 7. (top) The acoustic backscatter intensity (0–50 m); dots represent the location of Chameleon profiles in time and the depth of a density interface specified as the mean value over the range  $\sigma_\theta = 24\text{--}25.2$ ; gray and black dots indicate the locations of profiles shown in Fig. 8. The black dot indicates the profile from which an inferred velocity profile is combined with the measured density profile as input to a linear stability analysis in section 5. (bottom five) Potential temperature ( $\theta$ ), squared buoyancy frequency ( $N^2 = -g/\rho \times \rho_z$ , averaged vertically over 0.1 m), Thorpe scale  $L_T$ , temperature derivative ( $T'$ ), and  $\epsilon$ . The ordinate represents the distance both above and below the interface denoted by the dots in the top.

erated by shear instability, but on scales too small for the individual billows to be resolved. The sequence of flow states shown in Figs. 9 and 11 is qualitatively consistent with overturning and breaking due to shear instability. If this instability mechanism is to be consistent with the observational evidence, the instabilities

must grow rapidly enough to overturn and break within a small fraction (tens of seconds) of the wave period and wavelengths must be small enough that they are indistinguishable as individual billows in echosounder images (less than a few meters).

The potential of a given flow to develop shear insta-

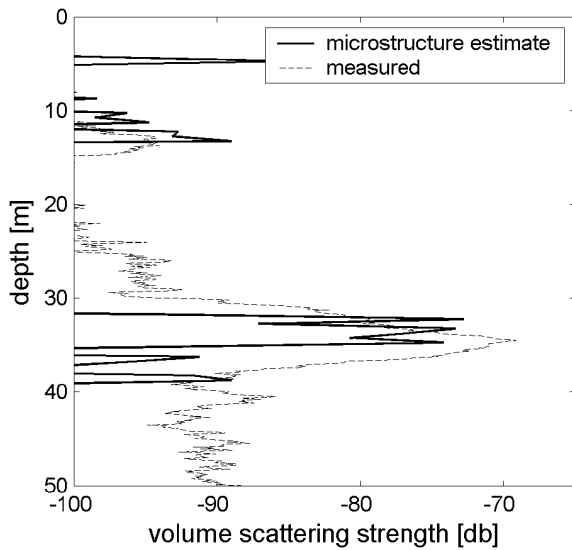


FIG. 10. Volume scattering strength. The dotted line is the measured echosounder target strength. The black line is estimated from temperature and salinity microstructure measurements from the profile represented by the final gray dot on Fig. 9. The high measured backscatter at the interface between 30- and 40-m depth and trailing the wave trough is represented well by the microstructure estimate.

bility is diagnosed with the gradient Richardson number, defined as  $Ri = N^2/(U_z^2 + V_z^2)$ , where  $U_z$  and  $V_z$  are the vertical shears of the horizontal components of velocity. If  $Ri < 1/4$  somewhere in the region of interest, the potential for shear instability exists (Howard 1961). Observed profiles of velocity and density in the ISW at the point of incipient interface instability (the black dot in Fig. 9) are shown in Fig. 15. The mismatch in vertical resolution is obvious in the figure. The in situ density profile from Chameleon resolves vertical scales of a few centimeters. However, the ADCP is a remote measurement of velocity, requiring the combination of range-gated signals from four slanted beams to achieve a single velocity estimate. In contrast to our density measurement, the result is heavily averaged both vertically and horizontally. As well, the two measurements do not sample the same location. The ADCP was mounted near to midship while Chameleon was deployed from the stern, about 15 m aft, and is carried some unknown lateral distance by the currents as it profiles.

Combining observed velocity and density measurements at the interface at 30 m, we find that  $Ri > 1$ . On this basis, we would conclude that the flow is dynamically stable. Yet, we clearly observe turbulence devel-

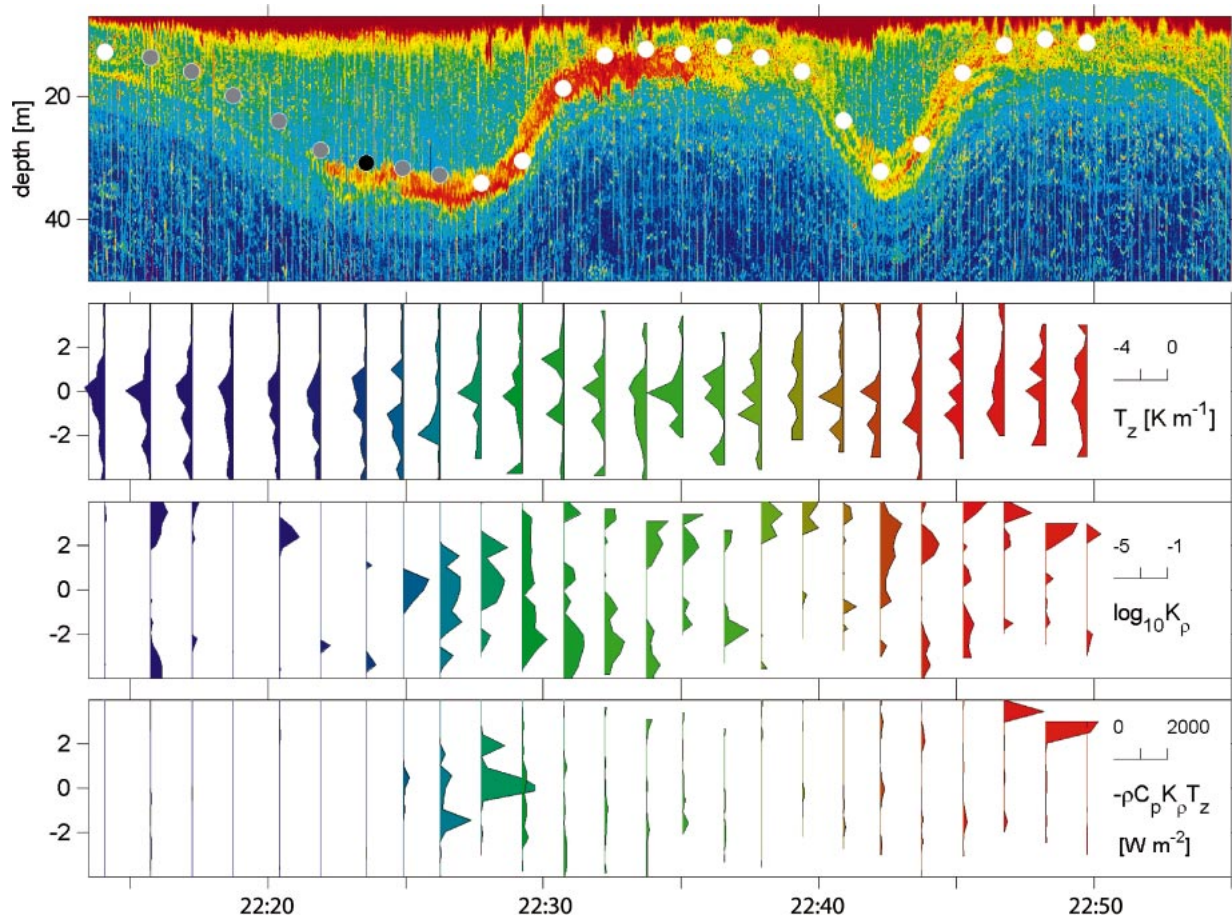


FIG. 11. Turbulent diffusivities and heat fluxes through the interface documented in Fig. 9.

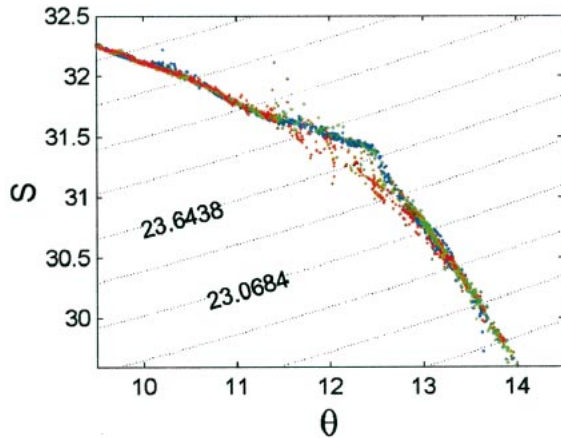


FIG. 12. The  $\theta$ - $S$  curves ahead of (blue), through (green), and trailing (red) an ISW similar to that in Fig. 9.

oping in a manner otherwise consistent with shear instability. We are thus led to consider the possibility that our estimate of  $Ri$  is too large because of underresolution of the velocity profile. While we cannot directly observe currents on scales less than a few meters, we will advance and test a hypothesis for their form and origin.

In a wave propagating without change of form, mass conservation dictates that the localized compressive strain needed to sharpen a density interface (lower layer in Fig. 16a) must act similarly on streamlines calculated in the wave's reference frame (Fig. 16b). The result is that the upper layer (in which stratification is reduced) is accelerated in the direction of the wave's propagation, while the lower layer (the sharpened density interface) is accelerated in the opposite direction. The shear between these adjacent currents results in local reductions of  $Ri$  and, potentially, in instability. Our density profiles indicate that such regions of locally accelerated fluid would be confined to vertical scales of no more than a few tens of centimeters and would therefore be invisible to the ADCP.

Coincident compression of isopycnals and streamlines may have an amplified effect on  $Ri$ . If we consider the horizontal velocity as the vertical derivative of the streamfunction,  $u = -\psi_z$ , then the velocity shear is  $-\psi_{zz}$ . A difference form of  $Ri$  is

$$Ri_{\Delta} = -\frac{g}{\rho} \frac{\Delta\rho}{\Delta U^2} \Delta z = \frac{g}{\rho} \frac{\Delta\rho}{\Delta^2\psi} \Delta z^3, \quad (2)$$

where  $\Delta\rho$  and  $\Delta U$  represent differences between a fixed pair of isopycnals with instantaneous spacing  $\Delta z$ ,  $\Delta^2\psi$  represents a second difference between three streamlines with the same spacing, and  $Ri_{\Delta}$  varies as the cube of the interface thickness,  $\Delta z$ . Simultaneous, compressive straining (reduction of  $\Delta z$ ) of both density and velocity will act to reduce  $Ri$  rapidly relative to  $\Delta z$ . Further discussion of wave straining and shear instability in solitary waves may be found in Farmer and Smith (1978).

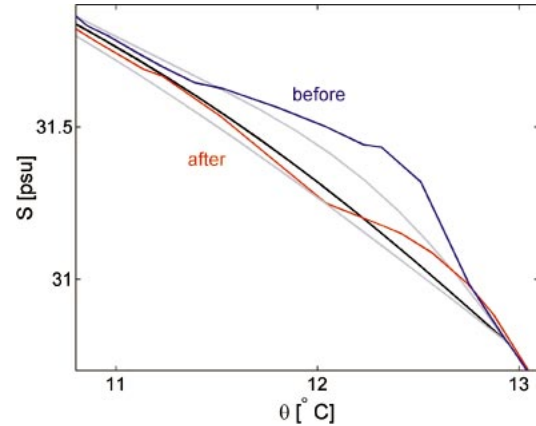


FIG. 13. The  $\theta$ - $S$  curves upstream (before) and downstream (after) of an ISW. These correspond to the initial and final curves shown in Fig. 12. The black line is the result of numerical solution of a time-dependent diffusion equation ( $K_p = 0.005$ ) with the blue curve as the initial condition, as described in the text. The two gray lines represent bounds on the calculation that were reproduced with  $K_p = [0.001 \text{ } 0.01]$ .

In the following two sections, we discuss this mechanism in detail and suggest that it could account for the observed turbulence.

#### a. Inferring a velocity profile

In a two-dimensional, nondiffusive wave that propagates at a fixed speed without change of shape, the velocity field can be determined from the density field using the fact that, in a reference frame following the wave, streamlines are everywhere parallel to isopycnals. Since the observed waves are approximately two-dimensional and move with well-defined phase velocity, we conjecture that the velocity field within these waves may be deduced in the same way.

Density and velocity fields are considered to be composed of three components:

- 1) an ambient state that varies only in the vertical;
- 2) a two-dimensional wave propagating without change of form at a constant, known phase velocity  $c_w$ ; and
- 3) turbulent fluctuations (i.e., everything else).

We now make the following three assumptions.

- 1) The turbulence component involves density fluctuations smaller than a specified magnitude  $\Delta\rho$ , so that averaging the data into isopycnal bins of size  $\Delta\rho$  leaves only the ambient profile plus the wave.
- 2) The wave is nondiffusive from its leading edge to the point at which turbulence appears (roughly the wave trough).
- 3) The ambient profiles of density and velocity are those measured just before the isopycnals begin to descend.

These assumptions allow us to infer the velocity profile at any location within the leading half of the wave

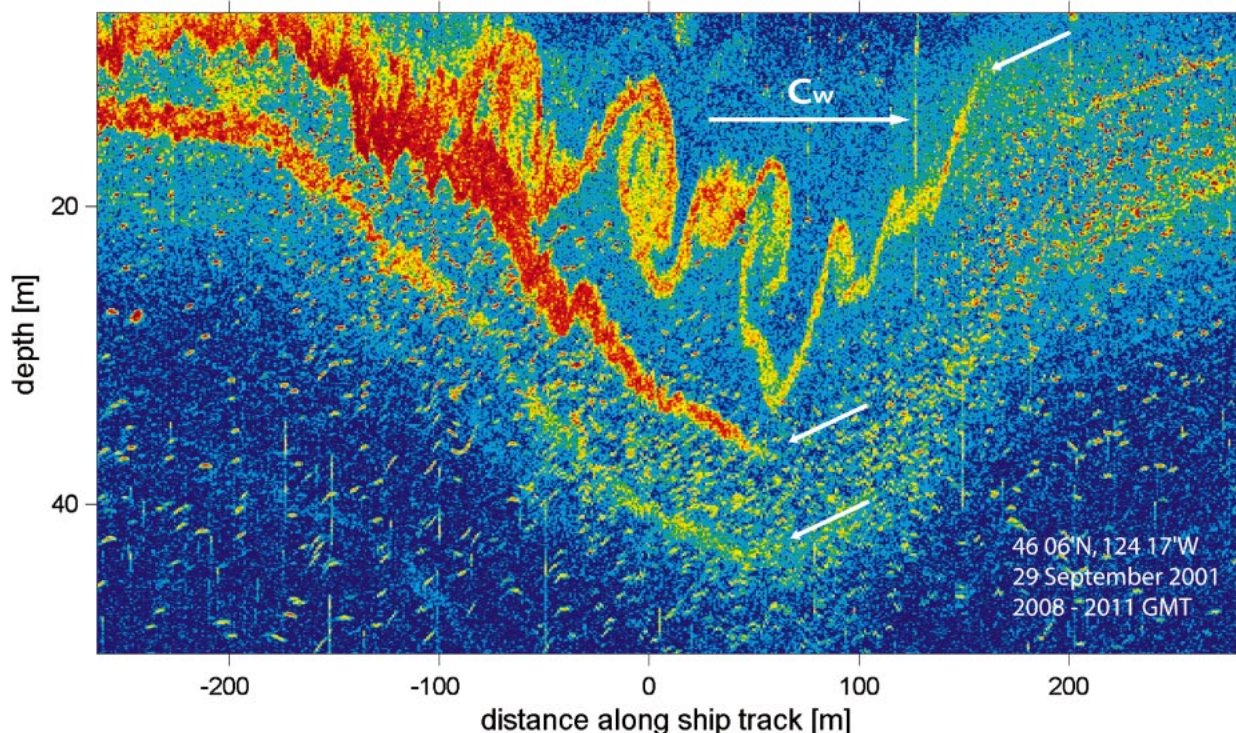


FIG. 14. Example acoustical snapshot of a propagating ISW within which is embedded a sequence of rollups identical in nature to Kelvin–Helmholtz instabilities observed in the laboratory and in small-scale simulations. The vertical scale of the largest is more than 10 m, and the horizontal scale (in the direction of wave propagation) is about 50 m. Toward the trailing edge of the wave, the rollups become less coherent but contribute a greater backscatter signal, suggesting breakdown to turbulence. At greater depth, denoted by arrows, are two more layers of bright backscatter. These are presumably the same phenomenon, but smaller scale. Hence the echosounder resolution does not permit a clear depiction of rollups.

given the density profile at the same location. First, the ambient streamfunction in the wave’s reference frame is obtained from the measured upstream velocity profile  $u_0(z)$  using

$$\psi_0(z) = - \int^z [u_0(z') - c_w] dz'. \quad (3)$$

At any location within the wave, we obtain the streamfunction profile corresponding to the local density profile  $\rho_1(z)$  using

$$\psi_1(\rho_1) = \psi_0(\rho_0). \quad (4)$$

Last, we differentiate<sup>5</sup> to obtain the velocity profile and transform into the earth’s reference frame:

$$u_1 = - \frac{\partial \psi_1}{\partial z} + c_w. \quad (5)$$

An appropriate value for  $\Delta\rho$  was obtained by examining density fluctuations in six profiles prior to and including the profile selected for analysis. Thorpe re-ordering was used to estimate density fluctuations in turbulent overturns. The maximum fluctuation had absolute value of  $0.1 \text{ kg m}^{-3}$  (Fig. 17). We adopted this

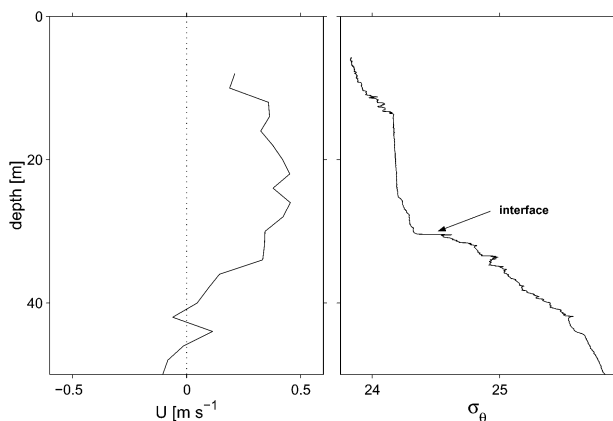


FIG. 15. (left) Observed profiles of horizontal velocity from 300-kHz ADCP (2-m bin size) and (right)  $\sigma_\theta$  from Chameleon. These coincide with the Chameleon profile noted by the black dot in Fig. 9 which corresponds to the time of maximum stratification at the interface at 30-m depth, after which overturns and intense turbulence first appear.

<sup>5</sup> Differentiations and integrations were approximated using second-order, finite differences on an uneven grid. Interpolations between the various data grids were done using an equal mixture of linear and cubic Hermite interpolants. (This controls the spurious peaks that appear when cubic interpolation is used alone.)



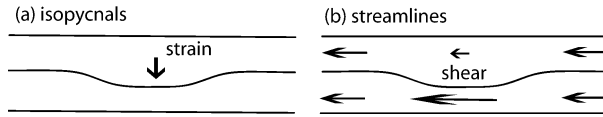


FIG. 16. Schematic showing the effect of a small-scale strain acting simultaneously on (a) isopycnals and (b) streamlines to generate a localized shear.

value for  $\Delta\rho$  but also tested the effects of using other values.

When applied to the case described in detail in section 4 (Figs. 7–11), this procedure yields the results shown in Fig. 18. To define the initial state, we averaged three successive profiles along with coincident ADCP velocity profiles, taken just before the isopycnals started to descend. Velocity profiles were averaged into depth-time bins of thickness 2 m and duration 60 s. The time interval for each bin began at the start time for the corresponding microstructure profile. This choice removed any bias due to the spatial separation between Chameleon and ADCP. Density profiles were sorted and averaged in bins of  $\Delta\rho = 0.1 \text{ kg m}^{-3}$ . The physical thicknesses of the density bins ranged from 20–30 cm in the thin layer of strong stratification to 6–7 m in weakly stratified regions. Conditions within the wave were represented by the single profile denoted by the black dot in Fig. 9, and the corresponding ADCP velocity profile. The inferred velocity profile within the wave was obtained using the procedure described above, with the wave's phase speed set to the measured value,  $c_w = 0.6 \text{ m s}^{-1}$ .

Density profiles measured upstream and within the wave show the downward displacement of isopycnals characteristic of an ISW of depression. The wave strain parameter

$$\gamma = \frac{\partial\rho/\partial z}{\partial\rho_0/\partial z} \quad (6)$$

(Fig. 18) indicates that isopycnals are generally being spread over the measured part of the water column, but thin layers located at 30, 34, and 39 m are compressed. In particular, the stratified layer near 30-m depth is compressed by nearly a factor of 2. Over the same time interval, the velocity profile measured by the shipboard ADCP (Fig. 18b, solid curve) evolves from near zero to a form resembling the first baroclinic mode, with flow in the direction of wave propagation above 40 m and a compensating flow at depth (the depth of the water column here is 99 m; Fig. 7). The inferred velocity profile (dashed curve in Fig. 18b) broadly resembles the measured profile within the wave. The primary difference between measured and inferred velocity profiles is the small-scale structure in the inferred profile, a direct result of the small-scale straining effect of the wave (as depicted in Fig. 16). In particular, the thin region of enhanced stratification near 30-m depth is accompanied by a similarly thin layer of fluid that has been accel-

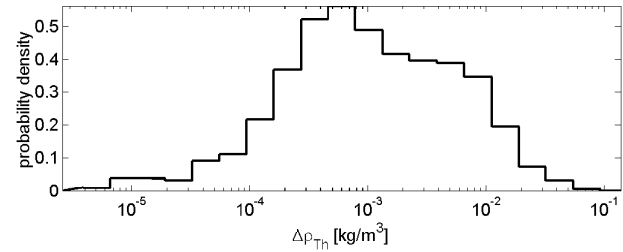


FIG. 17. Histogram of density fluctuations from the six profiles immediately preceding and including the black dot in Fig. 9. These were determined as the differences between observed and Thorpe-reordered profiles.

erated by the compressive wave strain to move opposite to the direction of the wave's propagation. The edges of this thin layer of locally accelerated fluid represent regions of high shear that could not be detected in our observations. We suggest that the thin layer of turbulence visible in the echosounder images is driven by the instability of these thin shear layers.

#### b. Linear stability analysis

To assess the potential of a flow structure like that shown in Fig. 18 to develop turbulence, we employ the well-known methods for stability analysis of a stratified parallel shear flow based on the Taylor–Goldstein equation. This requires the assumption that unstable modes are short in comparison with the horizontal scale of the ISW, so that the curvature of the streamlines and isopycnals can be neglected. The subsequent analysis is equivalent to that used by Sun et al. (1998) to assess the stability of measured equatorial currents, although the numerical methods employed here are different. Unstable perturbations are assumed to have a normal-mode

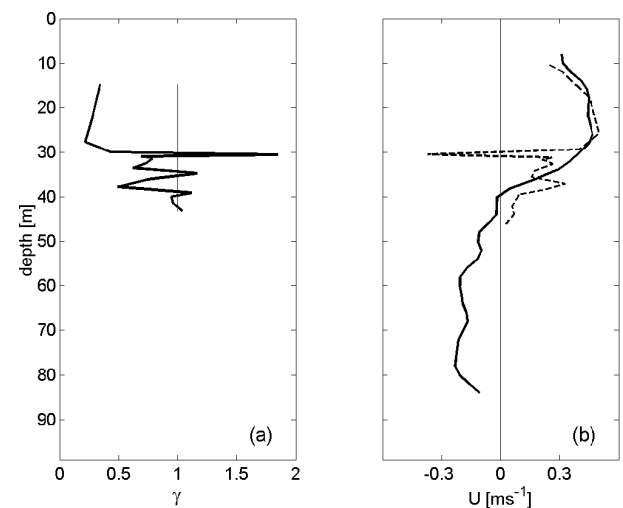


FIG. 18. (a) Strain parameter  $\gamma$  computed from Eq. (6) using binned density profiles. (b) Velocity profiles corresponding to the density profiles in (a). Thin dashed curve: inferred velocity within the wave  $u_1$ . Solid curve: observed ADCP velocity profile.

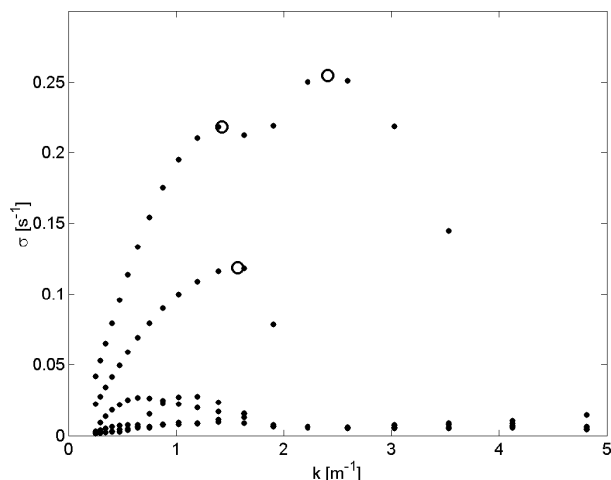


FIG. 19. Growth rate vs wavenumber for the inferred flow shown in Fig. 18. Units are radian frequency and radian wavenumber. Three prominent maxima are highlighted by circles.

form characterized by a horizontal wavenumber  $k$ , an exponential growth rate<sup>6</sup>  $\sigma$ , and a phase velocity  $c_r$ , and  $\sigma$  and  $c_r$  are obtained as functions of  $k$ . Details of this procedure are given in the appendix.

We begin by interpolating the profiles onto a grid of depths  $z_i$  chosen to give the high vertical resolution needed for accurate numerical solution of the equation. Two hundred points were chosen, concentrated in the region of strong shear in accordance with

$$(z_{i+1} - z_{i-1})^{-1} \propto \text{sech}^2 \frac{z_i - z_0}{\delta}. \quad (7)$$

The parameter  $z_0$  is computed as the mean of  $z$  weighted by

$$W(z) = \max(|\partial u / \partial z| - 2N, 0), \quad (8)$$

and  $\delta$  is the root-mean-square deviation of  $z$  weighted in the same way. (The weighting function approximates the dependence of shear instability growth rates on local shear and stratification.) For the example shown in Fig. 18,  $z_0$  corresponds to 30-m depth and  $\delta = 9$  m.

Eigenfunctions of the Taylor–Goldstein equation are then obtained for numerous values of  $k$ , and those corresponding to local maxima of  $\sigma(k)$  are identified. Each mode is then assessed for its ability to grow to finite amplitude during the passage of the ISW. This depends not only on the growth rate but also on the time the mode spends within the portion of the ISW where shear is strong. To address this issue rigorously would require that the normal-mode assumption inherent in the stability analysis be abandoned and a more general initial value problem be solved. For the present analyses, a simpler approach is taken. If the length of the sheared

<sup>6</sup> The growth rate  $\sigma$  should not be confused with the potential density  $\sigma_\theta$ .

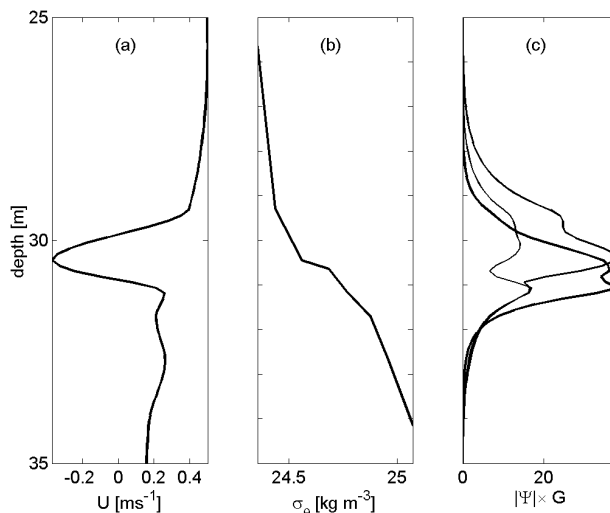


FIG. 20. (a) Inferred velocity. (b) Density. (c) Eigenfunctions of the three dominant modes from Fig. 19. Each eigenfunction is normalized by the growth factor  $G$ .

part of the ISW is estimated as  $L$ , then the time the mode has to grow is  $L/|c_w - c_r|$ , and

$$G = \sigma L / |c_w - c_r| \quad (9)$$

is an estimate of the number of  $e$ -foldings the mode may undergo during the passage of the wave. We set  $L$  to 100 m, which represents about 1/2 the length of the ISW we have chosen as our example (Fig. 5). If  $G$  is not significantly greater than unity for a given mode, we conclude that the emergence of strong turbulence due to that mode is unlikely, however large the growth rate may be. Note that modes whose phase speeds are close to  $c_w$  have the potential to grow to large amplitude even if their growth rates are not large. In contrast, a mode growing on a reversed current like that shown in Fig. 18 is likely to have phase speed very different from (or even of opposite sign to)  $c_w$ . Such a mode must grow rapidly if it is to generate turbulence.

Figures 19 and 20 show results for the density and inferred velocity profiles in Fig. 18. The growth rate (Fig. 19) exhibits three prominent maxima. These modes have wavelengths between 3 and 4.5 m and phase velocities between  $-0.10$  and  $0.05$  m s<sup>-1</sup>. These wavelengths are small enough that their billow structure would be smeared in the echosounder images at 30 m range. Figure 20c shows eigenfunctions normalized by values of the growth factor  $G$ . All of these modes are concentrated between 29- and 32-m depth, coinciding closely with the layer in which strong turbulence was observed to develop. Two of these modes have a double-peaked structure characteristic of a jet instability, while the third is a Kelvin–Helmholtz-like mode focused on the upper shear layer. The two strongest modes have growth factors near 30 and are therefore expected to grow to large amplitude as the ISW passes. In summary, the results of the linear stability analysis are consistent

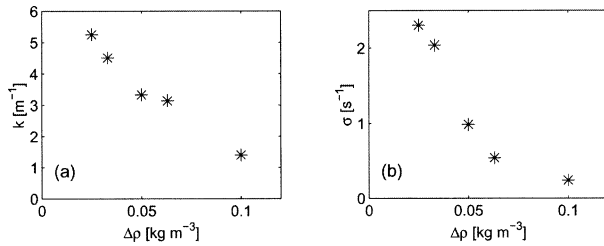


FIG. 21. (a) Wavenumber and (b) growth rate of the most unstable mode as functions of the bin size  $\Delta\rho$ .

with our proposed interpretation of the observations: normal modes are small enough to be undetectable in the echosounder data and unstable enough for their energy to grow by many orders of magnitude during the passage of the soliton.

The scale of the inferred velocity fluctuations is sensitive to our choice of the binning interval  $\Delta\rho$ . Smaller values of  $\Delta\rho$  yield larger velocity fluctuations and hence stronger instability. The dependence of the stability characteristics of the mode having maximum growth factor upon the bin size is illustrated in Fig. 21. As expected, decreasing bin size leads to increasing wavenumber (Fig. 21a) and increasing growth rate (Fig. 21b). However, reducing  $\Delta\rho$  also increases the likelihood that the density structure attributed to the wave is contaminated by turbulent fluctuations, which in turn would violate one of the key assumptions we have made in inferring the velocity profile.

The analyses described above pertain only to the case selected for detailed discussion in section 4 (e.g., Figs. 9 and 11). Several other cases have been examined with similar results: under the assumptions given in section 5a, the local compression of isopycnals observed during ISW passage implies intense, small-scale shears and correspondingly intense, small-scale instabilities.

### 6. Discussion

Our impression of the internal structure of these ISWs comes from the high vertical resolution in density we are able to measure from Chameleon profiles and the

continuous record of acoustic backscatter we obtain from a hull-mounted, high-frequency echosounder. The salient features are summarized in Fig. 22. The large vertical displacement of isopycnals associated with this wave of depression is primarily mode 1. The more subtle strain depicted by the compression of the interior two isopycnals as they plunge immediately ahead of the wave trough. At or near the wave trough, turbulence is first observed as 1) unstable overturns in density, 2) enhanced temperature microstructure, and 3) high values of  $\epsilon$ . If, as we have assumed, streamlines follow isopycnals ahead of the wave trough (before turbulence is triggered) then streamlines are also compressed. The consequence is a thin layer of accelerated fluid, above and below which the vertical gradient of velocity is high, perhaps sufficient to initiate shear instability with growth rates high enough that instability occurs before the wave passes and wavelengths small enough that instability waves are typically not detected by our acoustics. The trailing edge and wake of the wave are marked by high acoustic backscatter, which we have associated with the sound speed fluctuations induced by enhanced density microstructure.

By mixing the interface, each wave modifies the upstream condition for the next wave in the sequence and for the next wave train to propagate through that particular patch of fluid. This in turn will alter both the wave propagation characteristics and the characteristics of small-scale instabilities generated in the following waves.

The sequence shown in Figs. 3, 5, and 6 gives a clear depiction of the acoustic backscatter structure at the compressed interface. Although this signature becomes obscured by preexisting scatterers as the waves propagate farther onshore, the high-density microstructure and dissipation at the interface persist over at least 20 km (10 h). This persistence timescale is much greater than the inverse growth rate of predicted instabilities, the decay timescale of the turbulence, and the advective timescale of the ISWs. Hence, we conclude that these ISWs are continually triggering instabilities as they propagate.

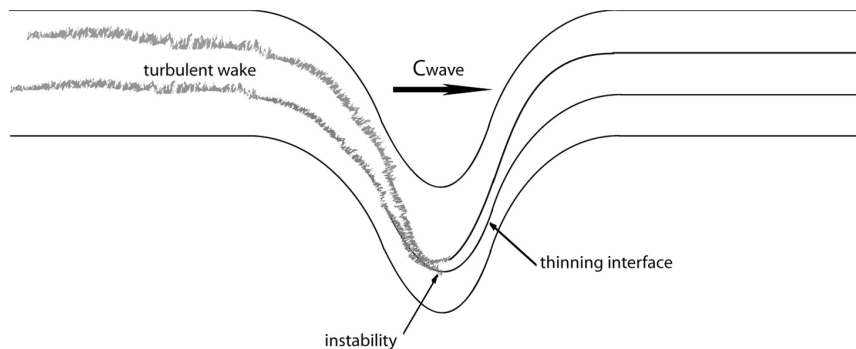


FIG. 22. Summary schematic of the evolving structure of isopycnals with the passage of an internal solitary wave propagating to the right.

The interfacial structure we have described is, while not ubiquitous, quite typical of the ensemble of observations. It also seems that the ISWs described here are similar in nature to the equatorial solitary waves observed in deep water by Pinkel (2000). Although Pinkel (2000) did not have detailed microstructure and turbulence observations, the basic structure of the acoustic backscatter is identical to that described here.

A laboratory study of breaking ISWs in a background flow that is broadly similar to that found in our observations—that is, a surface stratified layer overlying a layer of mixed fluid—has recently been reported by Grue et al. (2000). They found that breaking occurs in ISWs whose amplitude is as small as one-half of the thickness of the surface stratified layer. The breaking took the form of vortices that formed at the leading edge of the ISW. Breaking was more pronounced in larger-amplitude waves. The scenario that emerged in the laboratory experiments closely resembles the observations shown in Fig. 14. However, Grue et al. (2000) found that measured values of the gradient Richardson number exceeded 1/4. They therefore rejected shear instability as a mechanism for breaking and instead suggested an explanation based on surface tension. On the scale of ocean ISWs, surface tension is not expected to be a significant factor, and the observed form of the vortices clearly suggests shear instability. It is possible that Grue et al. (2000)'s direct measurements of the Richardson number were inaccurate because of underresolution of the velocity field, just as we find in our own data, in which case the turbulence may have been caused by shear instability after all. It is equally possible that the laboratory ISWs became turbulent through a different mechanism than that at work in the ocean.

The idea that a highly nonlinear internal wave may exhibit vertical structure on scales much smaller than its dominant mode (mode 1 in this case) diverges from the standard picture of internal solitons. We should not expect that standard picture to hold in detail, however, because the amplitude of these waves is far beyond the domain of validity of the low-order soliton models upon which it is based.

The small-scale velocity structure we have inferred is based upon a reasonable assumption about the coincidence of streamlines and isopycnals before the onset of turbulence. Small-scale velocity structure similar to this has been observed in the summer thermocline at about 20-m depth in the Mediterranean Sea off Malta in thin sheets of strong temperature gradient (Woods 1968). Successive underwater photographs of a vertical streak of dye indicate a steady distortion of the streak over 15 s corresponding to a steady shear of  $0.1 \text{ s}^{-1}$  over a 0.1-m-thick sheet. While the larger-scale processes contributing to that small-scale structure cannot be clearly identified from the data given, the latter is remarkably similar to the structure inferred from our observations.

The present observations do not include a measure-

ment of small-scale and steady velocity structure. While we do have a measure of the random, isotropic velocity shears that characterize turbulence (using airfoil probes), the technique is not well-suited for detecting the predicted coherent flow structure, and our attempts to identify this velocity structure in the data are thus far inconclusive. Confirmation of this instability mechanism within ISWs must await more suitable velocity measurements.

The use of the Osborn (1980) formulation for  $K_p$  with  $\Gamma = 0.2$  may be oversimplified for this application. Direct numerical simulations of instabilities evolving through to decaying turbulence indicate an evolution of the mixing efficiency as well (Smyth et al. 2001; Winters et al. 1995; Caulfield and Peltier 2000; Staquet 2000). At early preturbulent stages of the instability (before we might recognize this as turbulence from field observations), small-scale stirring creates large temperature gradients and enhanced mixing efficiency [ $O(1)$ ], following which  $\Gamma \rightarrow 0.2$  as the turbulence decays. It was noted by Smyth et al. (2001) that the ratio  $L_0/L_T$  was a good indicator of the time in the evolution of the instability and hence of  $\Gamma$ . At early stages,  $L_0/L_T \ll 1$ , but  $L_0/L_T \rightarrow 1$  as turbulence develops. We have suggested that our observations include the turbulence that is newly generated, the implication being that the mixing at this stage may be significantly more efficient than we have assumed. A consequence would be greater heat flux through the interface than we have estimated.

## 7. Conclusions

We have observed large-amplitude (40 m), strongly nonlinear internal solitary waves of depression over the continental shelf off Oregon just south of the Columbia River and inshore of its plume. These waves propagate onshore at about  $0.6\text{--}0.8 \text{ m s}^{-1}$ . Propagation directions were observed to be  $090 \pm 25^\circ$ . Radar and visual observations indicate that, on scales of many tens of wavelengths perpendicular to their fronts, these waves are roughly two-dimensional.

Particularly large instabilities are wonderfully visible in acoustic images. The example of large KH-like billows shown in Fig. 14 is characterized by vertical scale 10 m and horizontal scale (in the direction of propagation) 50 m. Presumably these are aligned with wave fronts, which are linear on scales of several kilometers (Fig. 2), suggesting that the longitudinal scale of the billows may be  $O(\text{km})$ . In general, however, such clearly observable instabilities are rare. The small wavelength instabilities we have proposed would be blurred by the finite echosounder beamwidth.

While the distortion of acoustic scattering layers, isopycnals, and streamlines is predominantly first mode, there is significant small-scale straining as well. Our results suggest that this small-scale straining is responsible for instability in the ISWs. High acoustic backscatter observed along strained interfaces at the wave

crests, trailing edges, and wake but not at the leading edge is clearly associated with enhanced density microstructure. This indicates the highly turbulent nature of the waves.

The sequence of events observed at the interface begins with enhanced  $N^2$  ahead of the wave crest due to compressive strain, followed by overturns, and finally by enhanced density microstructure and high  $\varepsilon$ . These interfaces are characterized by strong mixing. Local (or instantaneous) heat fluxes are  $O(kW\ m^{-2})$ . The modification of the interface by mixing changes the upstream condition for the next wave.

By assuming that streamlines parallel isopycnals, we have inferred a small-scale velocity structure that we are unable to observe directly but is consistent with the nature of the ISW ahead of the wave crest. The existence of this velocity structure implies shear instabilities with growth rate timescales of tens of seconds or less and wavelengths of meters or less. This would account for the apparently *spontaneous* generation of turbulence at the interfaces in cases in which we cannot observe the instability leading to turbulence.

*Acknowledgments.* This work was funded by the Office of Naval Research. We are grateful to the captain, crew, and marine technician of R/V *Wecoma* for tolerating our continually evolving sampling strategies and for permitting us to control and photograph the ship's X-band radar. We acknowledge the assistance of Mike Neeley-Brown, Ray Kreth, Greig Thompson, Nick Hall-Patch, and Peter Chandler in obtaining the data. Jody Klymak and Sasha Perlin made important contributions to the early analysis.

## APPENDIX

### Normal-Mode Stability Analysis of Parallel, Stratified Shear Flow

We assume that the background flow is purely horizontal and that the density distribution is Boussinesq. Both velocity and density vary only in the direction parallel to gravity, so that

$$U = U(z) \quad \text{and} \quad N = N(z), \quad (\text{A1})$$

where  $N$  is the buoyancy frequency associated with the background stratification. For the present application, we assume that the instabilities of interest are two-dimensional; that is, they do not vary in the spanwise ( $y$ ) direction.

The linearized evolution equations for two-dimensional perturbations to a stratified, parallel shear flow are written as

$$\begin{aligned} \frac{\partial \xi}{\partial t} &= -U\xi_x + U_{zz}\psi_x + b_x, \\ \frac{\partial b}{\partial t} &= -Ub_x - N^2\psi_x, \quad \text{and} \\ \nabla^2\psi &= \xi. \end{aligned} \quad (\text{A2})$$

Here,  $\xi(x, z, t)$  is the spanwise vorticity associated with the perturbation,  $\psi(x, z, t)$  is the corresponding streamfunction, and  $b = -g\rho/\rho_0$  is the buoyancy ( $\rho_0$  is a constant, characteristic value for the density).

Because the background flow depends only on  $z$ , disturbances may be expanded into normal modes characterized by a horizontal wavenumber  $k$  and phase velocity  $c$ , for example,

$$\psi(x, z, t) = \hat{\psi}(z)e^{ik(x-ct)}, \quad (\text{A3})$$

in which  $\hat{\psi}$  is a complex structure function. (Ultimately, only the real part of  $\psi$  is physically relevant.) For the present application, the wave vector is assumed to be real, but the phase velocity is allowed to be complex. A nonzero imaginary phase velocity describes temporal growth or decay. The normal-mode assumption allows us to convert (11) to the form of a differential eigenvalue problem equivalent to the Taylor–Goldstein equation:

$$\begin{bmatrix} U - U_{zz}\nabla^{-2} & -g \\ N^2\nabla^{-2} & U \end{bmatrix} \begin{pmatrix} \hat{\xi} \\ \hat{b} \end{pmatrix} = c \begin{pmatrix} \hat{\xi} \\ \hat{b} \end{pmatrix}. \quad (\text{A4})$$

As before, carets indicate  $z$ -dependent complex structure functions. The differential operator  $\nabla^{-2}$  represents the inverse of the Laplacian operator, that is,  $\nabla^2\hat{\psi} = (\partial_{zz} - k^2)\hat{\psi} = \hat{\zeta}$ , with the Dirichlet condition  $\hat{\psi} = 0$  at the upper and lower boundaries.

The  $z$  dependence is now discretized so that all functions have the form  $f_m = f(z_m)$ ;  $m = 1, 2, \dots, M$ , and a suitable finite approximation is chosen for the  $z$  derivatives. This converts  $\nabla^{-2}$  to an  $M \times M$  matrix. The result is a matrix eigenvalue problem of order  $2M$ . In the present calculations, the derivatives are approximated by third-order compact forms [an extension of the method of Lele (1992) for nonuniform grid spacing]. These have the virtue of maintaining high accuracy without requiring that the  $z$  values be evenly spaced.

Because the discrete eigenvalue problem solved here is an approximation to the continuous Taylor–Goldstein equation, one may hope that solutions of the former are approximations to solutions of the latter. Unfortunately, this is not true in general. In fact, the discrete problem has  $2M$  solutions. Typically, only a few of these correspond to solutions of the continuous problem; the rest are artifacts of the discretization. These spurious modes are rejected by requiring that the kinetic energy equation be satisfied. The latter furnishes an alternative expression for the growth rate:

$$\sigma_k = \frac{S + B}{2K}, \quad (\text{A5})$$

where

$$\begin{aligned} K &= \int \frac{1}{2}(\psi_x^2 + \psi_z^2) dz, \quad S = \int U_z \psi_x \psi_z dz, \quad \text{and} \\ B &= \int \psi_x b dz, \end{aligned} \quad (\text{A6})$$

which must match  $\sigma$  to within 1%.

## REFERENCES

- Caulfield, C., and W. Peltier, 2000: Anatomy of the mixing transition in homogeneous and stratified free shear layers. *J. Fluid Mech.*, **413**, 1–47.
- Crawford, W. R., and R. K. Dewey, 1989: Turbulence and mixing: Sources of nutrients on the Vancouver Island continental shelf. *Atmos.–Ocean*, **27**, 428–442.
- DeSilva, I., H. Fernando, F. Eaton, and D. Hebert, 1996: Evolution of Kelvin–Helmholtz billows in nature and laboratory. *Earth Planet. Sci. Lett.*, **143**, 217–231.
- Duda, T. F., and D. M. Farmer, 1999: 1998 WHOI/IOS/ONR internal solitary wave workshop. Woods Hole Oceanographic Institution Tech. Rep. WHOI-99-07, 247 pp.
- Farmer, D. M., and J. D. Smith, 1978: Nonlinear internal waves in a fjord. *Hydrodynamics of Estuaries and Fjords*, J. C. J. Nihoul, Ed., Elsevier, 465–493.
- , and —, 1980: Tidal interaction of stratified flow with a sill in Knight Inlet. *Deep-Sea Res.*, **27A**, 239–254.
- Fu, L. L., and B. Holt, 1982: *Seasat* views oceans and sea ice with synthetic-aperture radar. NASA Jet Propulsion Laboratory Publication 81-120, 200 pp.
- Goodman, L., 1990: Acoustic scattering from ocean microstructure. *J. Geophys. Res.*, **95**, 11 557–11 573.
- Grue, J., A. Jensen, P. Rusas, and J. Sveen, 2000: Breaking and broadening of internal solitary waves. *J. Fluid Mech.*, **413**, 181–218.
- Howard, L., 1961: Note on a paper of John W. Miles. *J. Fluid Mech.*, **10**, 509–512.
- Kao, T., F. S. Pan, and D. Renouard, 1985: Internal solitons on the pycnocline: Generation, propagation and shoaling and breaking over the slope. *J. Fluid Mech.*, **159**, 19–53.
- Koop, C., and F. Browand, 1979: Instability and turbulence in a stratified layer with shear. *J. Fluid Mech.*, **93**, 135–159.
- Kropfli, R. A., L. A. Ostrovski, T. P. Stanton, E. A. Skirta, A. N. Keane, and V. Irisov, 1999: Relationships between strong internal waves in the coastal zone and their radar and radiometric signatures. *J. Geophys. Res.*, **104**, 3133–3148.
- Lamb, K. G., 1997: Particle transport by nonbreaking internal solitary waves. *J. Geophys. Res.*, **102**, 18 641–18 660.
- Lee, C., and R. Beardsley, 1974: The generation of lone nonlinear internal waves in a weakly stratified shear flow. *J. Geophys. Res.*, **79**, 453–462.
- Lele, S. K., 1992: Compact finite difference schemes with spectral-like resolution. *J. Comput. Phys.*, **103**, 16–42.
- Moum, J. N., 1996: Efficiency of mixing in the main thermocline. *J. Geophys. Res.*, **101** (C5), 12 057–12 069.
- , M. C. Gregg, R. C. Lien, and M. E. Carr, 1995: Comparison of turbulence kinetic energy dissipation rate estimates from two ocean microstructure profilers. *J. Atmos. Oceanic Technol.*, **12**, 346–366.
- Nash, J. D., and J. N. Moum, 2001: Internal hydraulic flows over the continental shelf: High drag states over a small bank. *J. Geophys. Res.*, **106**, 4593–4611.
- , D. R. Caldwell, M. J. Zelman, and J. N. Moum, 1999: A thermocouple probe for high-speed temperature measurement in the ocean. *J. Atmos. Oceanic Technol.*, **16**, 1474–1482.
- Osborn, T. R., 1980: Estimates of the local rate of vertical diffusion from dissipation measurements. *J. Phys. Oceanogr.*, **10**, 83–89.
- , and C. S. Cox, 1972: Oceanic fine structure. *Geophys. Fluid Dyn.*, **3**, 321–345.
- Pinkel, R., 2000: Internal solitary waves in the warm pool of the western equatorial Pacific. *J. Phys. Oceanogr.*, **30**, 2906–2926.
- Sandstrom, H., and N. S. Oakey, 1995: Dissipation in internal tides and solitary waves. *J. Phys. Oceanogr.*, **25**, 604–614.
- , J. A. Elliott, and N. A. Cochrane, 1989: Observing groups of solitary internal waves and turbulence with batfish and echosounder. *J. Phys. Oceanogr.*, **19**, 987–997.
- Seim, H. E., 1999: Acoustic backscatter from salinity microstructure. *J. Atmos. Oceanic Technol.*, **16**, 1491–1498.
- , M. C. Gregg, and R. T. Miyamoto, 1995: Acoustic backscatter from turbulent microstructure. *J. Atmos. Oceanic Technol.*, **12**, 367–380.
- Smyth, W. D., and J. N. Moum, 2000: Anisotropy of turbulence in stably stratified mixing layers. *Phys. Fluids*, **12**, 1343–1362.
- , —, and D. R. Caldwell, 2001: The efficiency of mixing in turbulent patches: Inferences from direct simulations and microstructure observations. *J. Phys. Oceanogr.*, **31**, 1969–1992.
- Stanton, T. P., and L. A. Ostrovsky, 1998: Observations of highly nonlinear internal solitons over the continental shelf. *Geophys. Res. Lett.*, **25**, 2695–2698.
- Staquet, C., 2000: Mixing in a stably-stratified shear layer: Two and three-dimensional numerical experiments. *Fluid Dyn. Res.*, **27**, 367–404.
- Sun, C., W. D. Smyth, and J. N. Moum, 1998: Dynamic instability of stratified shear flow in the upper equatorial ocean. *J. Geophys. Res.*, **103** (C5), 10 323–10 337.
- Sundermeyer, M. A., and J. R. Ledwell, 2001: Lateral dispersion over the continental shelf: Analysis of dye-release experiments. *J. Geophys. Res.*, **106** (C5), 9603–9621.
- Thorpe, S. A., and J. M. Brubaker, 1983: Observation of sound reflection by temperature microstructure. *Limnol. Oceanogr.*, **28**, 601–613.
- Vlasenko, V., and K. Hutter, 2002: Numerical experiments on the breaking of solitary internal waves over a slope-shelf topography. *J. Phys. Oceanogr.*, **32**, 1779–1793.
- Winters, K., P. Lombard, J. Riley, and E. D’Asaro, 1995: Available potential energy and mixing in density-stratified fluids. *J. Fluid Mech.*, **289**, 115–128.
- Woods, J. D., 1968: Wave-induced shear instability in the summer thermocline. *J. Fluid Mech.*, **32**, 791–800.